apoptotic muscle degeneration, defects in mitochondrial morphology and increased sensitivity to multiple stresses, including oxidative stress (Park et al., 2006; Clark et al., 2006). These data, along with the recessive nature of *PINK1* mutations, suggest that this form of familial PD is associated with the loss of PINK1 function.

On the other hand, Tang et al. (2006) showed that DJ-1, another protein causatively associated with familial PD, normally interacts with and stabilizes PINK1, and DJ-1 mutations that attenuate this interaction reduce the stability of PINK1. These findings suggest that protein–protein interactions between PINK1 and one or more unknown proteins could play a key regulatory role in affecting the activity and stability of PINK1. In the present study, therefore, we endeavored to isolate PINK1-binding partners using a combination of immunoprecipitation and mass-spectrometric analysis with the aim of obtaining additional information on the pathogenic features of PINK1 mutations. Our findings suggest that the stability of PINK1 is strongly affected by its interaction with Hsp90, and that inhibition of the PINK1–Hsp90 interaction might contribute to the pathogenesis of PD.

2. Materials and methods

2.1. Plasmids and antibodies

The coding region of human PINK1 was cloned using standard RT-PCR techniques. PINK1 mutants were generated using a QuikChange site-directed mutagenesis kit (Stratagene) according to the manufacturer's instructions. Wild-type and all mutant PINK1 cDNAs were cloned into the mammalian expression vector pcDNA3, which also contained the FLAG tag sequence at its 3′ terminal (pcDNA3-FLAG-C). Proper construction of all the plasmids was verified by DNA sequencing. Anti-FLAG (M2), anti-Hsp90 (H-114), anti-Cdc37 (C-11) and anti-HA (Y-11) Abs were purchased from Sigma or Santa Cruz.

2.2. Cell culture and transfection

COS7 and HEK293 cells were cultured in Dulbecco's modified Eagle's medium supplemented with 10% heat-inactivated fetal bovine serum (ICN Biomedical, Inc.), 50 U/ml of penicillin and 50 U/ml of streptomycin at 37 °C under an atmosphere of 95% air/5% CO_2. Plasmids encoding PINK1 cDNAs were transfected into cells using Lipofectamine or Lipofectamine 2000 (Invitrogen) according to the manufacturer's instructions.

2.3. Purification of PINK1-binding proteins

PINK1-FLAG-transfected HEK293 cells were homogenized in lysis buffer (20 mM Hepes [pH 7.4], 150 mM NaCl, 10% glycerol and 1% Triton X-100) supplemented with Complete Protease Inhibitors (Roche Diagnostics). The soluble fraction of the lysate was immunoprecipitated with anti-FLAG M2 agarose (Sigma) and then washed five times in lysis buffer without protease inhibitors. The fractions eluted with 200 μg/ml FLAG peptide were resolved by SDS-PAGE, after which the protein bands were stained with Coomassie Brilliant Blue (CBB) and excised for in-gel digestion.

2.4. Mass-spectral analysis

In-gel digestion was carried out as described by Mineki et al. (2002). Briefly, the excised protein bands were alkylated and then incubated with 12.5 ng/μl trypsin/100 mM NH_4HCO_3 overnight at 37 °C. The resultant tryptic peptides were extracted from the gel by successive incubations with (i) 50% CH_3CN/1% trifluoroacetic acid and (ii) 20% HCOOH/25% CH_3CN/15% isopropanol/40% H_2O. The extracts from each step were pooled and dried by vacuum centrifugation. For peptide mapping, we used a LCQ-Deca XP ion trap mass spectrometer with a nanoelectrospray ionization source (Thermo Electron Corp., Waltham, MA) combined with a reverse-phase capillary column (Cadenza C18, 2 mm × 50 mm, Microme BioResources, Inc., Auburn, CA) on a Magic 2002 high performance liquid chromatography system (Microme BioResources, Inc.). The MS spectra and MS/MS spectra data were collected using Xcalibur software (Matrix Science, London, UK). The data were analyzed for candidate sequences of PINK1-interacting proteins using MASCOT software (Matrix Science) with a public domain protein database (National Center for Biotechnology Information).

2.5. Treatment with Hsp90 and protease inhibitors

Geldanamycin (GA) and novobiocin were purchased from Sigma. Epoxomycin, benzyloxycarbonyl-Leu-Leu-Leu-aldehyde (MG132), pepstatin A and leupeptin were from Peptide Institute. GA (1 mM) was prepared in DMSO and used at a final concentration of 3 μM; novobiocin was prepared in water and used at a final concentration of 1 mM; MG132 (10 mM) was prepared in DMSO and used at a final concentration of 5 μM; epoxomycin (1 mM) was prepared in DMSO and used at a final concentration of 1 μM; leupeptin (1 mM) was prepared in water and used at a final concentration of 20 μM; and pepstatin (1 mM) was prepared in DMSO and used at a final concentration of 25 μM. Cells were exposed to drugs or vehicles 24 h post-transfection.

2.6. Degradation assay

COS7 cells were transiently transfected with wild-type or L347P PINK1-FLAG. Twenty-four hours after transfection, cells were treated with 100 μg/ml cycloheximide (CHX) to prevent protein synthesis, after which they were harvested in lysis buffer at the times indicated in Section 3. Protein concentrations were determined using a Coomassie Plus Protein Assay Reagent kit (Pierce), and equal amounts of protein were subjected to SDS-PAGE. The resolved proteins were transferred to PVDF membranes (Immobilon, Millipore) and analyzed by immunoblot analysis using anti-FLAG Ab, after which the bands were visualized using an enhanced chemiluminescence detection kit (Amersham Pharmacia).

3. Results

3.1. PINK1 forms a complex with both Hsp90 and Cdc37

To isolate PINK1-binding proteins, HEK293 cells were transiently transfected with C-terminal FLAG-tagged PINK1 (PINK1-FLAG), after which proteins in the cell lysates were immunoprecipitated using anti-FLAG M2 agarose, subjected to SDS-PAGE, and stained with CBB. As a control, the same purification procedure was undertaken with non-transfected HEK293 cells. We observed several bands in samples from PINK1-FLAG transfectants that were not discernable in the control sample (Fig. 1A). We then identified the proteins in those bands using standard tryptic peptide mass-spectrometric finger printing (Fig. 1B). Consistent with earlier results, two of the proteins were identified as PINK1, itself (Beilina et al., 2005; Silvestri et al., 2005; Petit et al., 2005; Park et al., 2006), while the others were identified as Hsp90, Hsp70 and Cdc37. Hsp90 and Cdc37 were previously reported to interact with a number of other protein kinases, including one encoded by the PD-related gene *LRRK2* (Gloeckner et al., 2006). We then confirmed the mass-spectral identification of PINK1-associated proteins by immunoblotting samples of the purified protein

Please cite this article in press as: Moriwaki, Y., et al., L347P PINK1 mutant that fails to bind to Hsp90/Cdc37 chaperones is rapidly degraded in a proteasome-dependent manner, Neurosci. Res. (2008), doi:10.1016/j.neures.2008.01.006

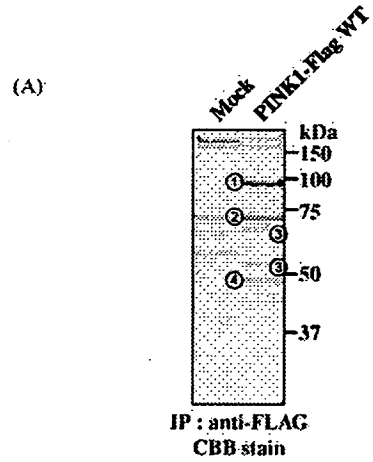

(B)

	Protein name	Score	% sequence converge
①	Hsp90	1623	56 %
②	Hsp70	720	34 %
③	PINK1	917	40 %
④	Cdc37	302	20 %

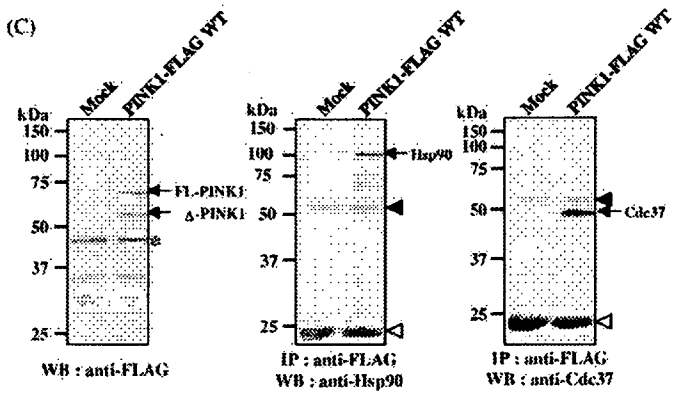

Fig. 1. PINK1 forms a complex with both Hsp90 and Cdc37. (A) HEK293 cells were transfected for 24 h with either a vector expressing PINK1-FLAG or with an empty vector (Mock). The transfectants were then lysed and immunoprecipitated with anti-FLAG Ab, the immunocomplexes were separated by SDS-PAGE, and the gel was stained with CBB to visualize proteins associated with PINK1. (B) CBB stained bands, labeled as indicated in (A), were excised from the gel and, following in-gel digestion with trypsin, their identities were determined by tryptic peptide mass-spectral fingerprinting. Scores and percentages of sequence converge for each protein identified are indicated. (C) The samples purified in (A) were immunoblotted with the indicated Abs; the asterisk indicates a non-specific band detected by anti-FALG Ab. Full length (FL) and processed PINK1 (Δ-PINK1) were detected. Closed and open arrowheads indicate IgG heavy and light chains, respectively.

with Abs against Hsp90, Cdc37 or FLAG (Fig. 1C). Taken together, these findings indicate that Hsp90 and Cdc37 specifically associate with PINK1.

3.2. Hsp90 regulates PINK1 stability

Hsp90 is a ubiquitous molecule that plays a key role in the stabilization and conformational regulation of various signaling effectors, including steroid hormone receptors and protein kinases (Young et al., 2001). To determine whether Hsp90 also regulates PINK1 stability, we next incubated COS7 cells transiently transfected with wild-type PINK1-FLAG with 1–10 μM GA, an inhibitor of Hsp90. We found that cells treated with 1 or 3 μM GA showed reduced levels of PINK1 (Fig. 2, top panel), whereas levels of Hsp90 and Cdc37 were unaffected (Fig. 2, middle and bottom panels). In addition, GA completely blocked the interaction between PINK1 and Hsp90/Cdc37. Examination of the time course of the response to GA revealed that levels of full-length PINK1 gradually declined by 90% over the course of 4 h after the addition of GA to COS7 cells (Fig. 3A). These findings were then confirmed using novobiocin, another known Hsp90 inhibitor that is structurally unrelated to GA and binds to the ATP-binding domain located in the C-terminal part of Hsp90 (Marcu et al., 2000). As shown in Fig. 3A, novobiocin treatment also significantly reduced levels of PINK1 in COS7 cells, and similar results were obtained with HEK293 cells (data not shown). The changes of PINK1 level induced by Hsp90 inhibitors are likely to be ascribable to its protein stability and degradation. First, PINK1 mRNA level was not affected by GA treatment as assessed by RT-PCR analysis (data not shown). Moreover, GA-induced PINK1 downregulation was suppressed by protease inhibitors (Fig. 3B).

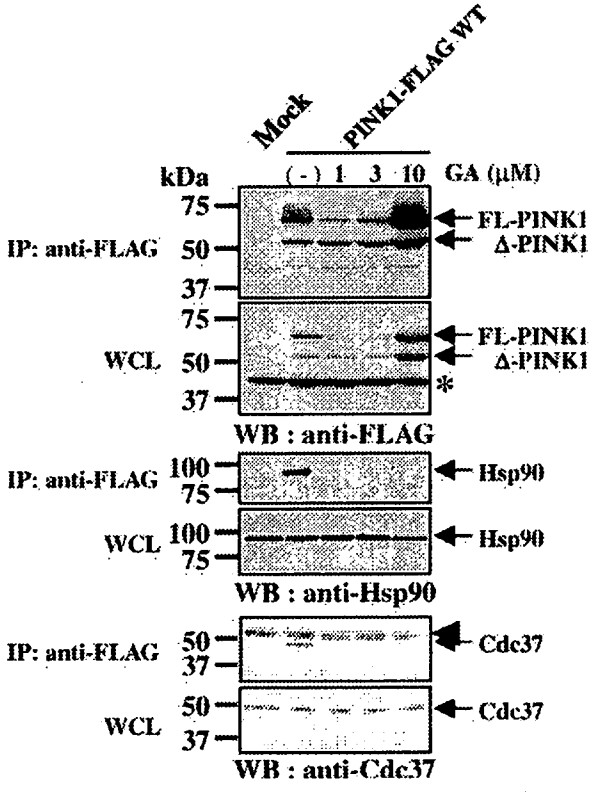

Fig. 2. GA treatment diminishes the interaction of PINK1 with both Hsp90 and Cdc37. COS7 cells were transfected for 24 h with either PINK1-FLAG or Mock expression vector and then treated with indicated concentration of GA. After incubating an additional 4 h, the cells were lysed and immunoprecipitated as described in Section 2. Immunocomplexes and whole-cell lysates (WCLs) were subjected to electrophoresis on polyacrylamide gel and immunoblotted with the indicated Abs; an asterisk indicates a non-specific band detected by anti-FALG Ab, which served as an internal control. The arrowhead indicates IgG heavy chain.

Please cite this article in press as: Moriwaki, Y., et al., L347P PINK1 mutant that fails to bind to Hsp90/Cdc37 chaperones is rapidly degraded in a proteasome-dependent manner, Neurosci. Res. (2008), doi:10.1016/j.neures.2008.01.006

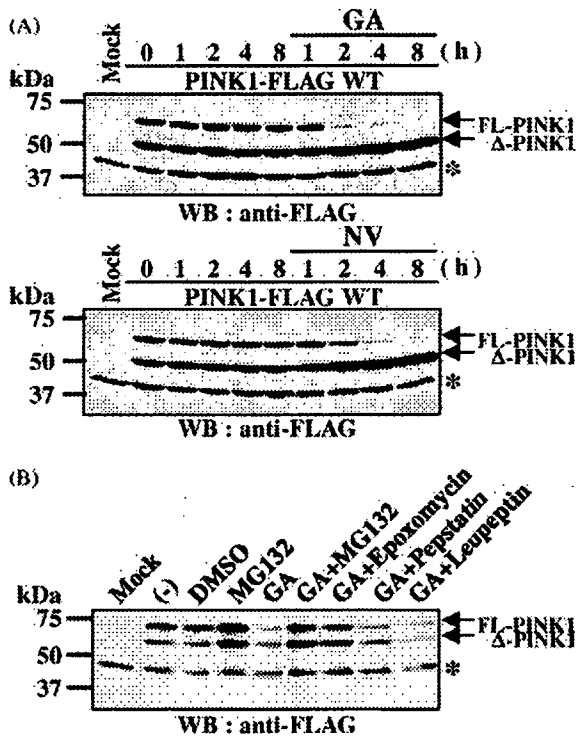

Fig. 3. PINK1 degradation is enhanced by Hsp90 inhibitors but inhibited by proteasome inhibitors. (A) COS7 cells were transiently transfected with PINK1-FLAG, after which the transfectants were incubated for the indicated times in the presence of 3 μM GA, 1 mM novobiocin (NV) or their vehicles (DMSO and water, respectively). After the indicated times or before the addition of drug (T0), the cells were lysed and their lysates were subjected to SDS-PAGE and immunoblotted with anti-FLAG M2 Ab. (B) COS7 cells transiently transfected with PINK1-FLAG were incubated for 4 h in the presence of GA or vehicle (DMSO). The proteasome inhibitors (epoxomycin or MG132) or lysosomal protease inhibitors (pepstatin or leupeptin) were simultaneously added in the presence or absence of GA. (−) indicates no drug treatment; the asterisk indicates a non-specific band detected by anti-FALG Ab, which served as an internal control.

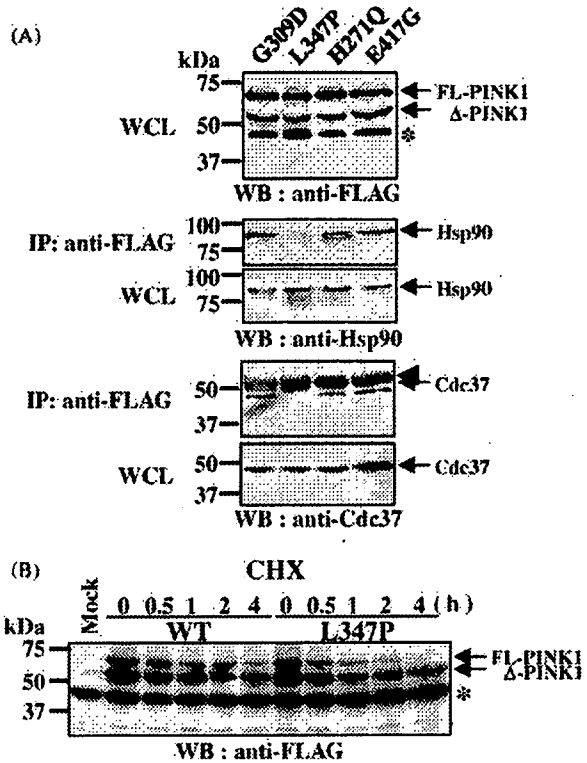

Fig. 4. Familial PD-associated L347P mutation impairs the interaction between PINK1 and Hsp90/Cdc37. (A) Wild-type PINK1 and PD-associated PINK1 mutants expressed in COS7 cells were immunoprecipitated with anti-FLAG Ab and immunoblotted with anti-Hsp90, anti-Cdc37 or anti-FLAG Ab. (B) COS7 cells were transfected for 24 h with either wild-type PINK1-FLAG or L347P mutant PINK1-FLAG, after which they were incubated for the indicated times in the presence of 100 μg/ml cycloheximide (CHX). After the indicated times or before the addition of CHX, cells were resuspended in lysis buffer, and the proteins were analyzed by immunoblotting using anti-FLAG M2 Ab. Similar results were obtained in two independent experiments. The asterisk indicates a non-specific band detected by anti-FALG Ab, which served as an internal control. The arrowhead indicates IgG heavy chain.

Several studies have shown that GA-induced degradation of Hsp90 target proteins is preceded by their ubiquitination and subsequent targeting by proteasome (Miyata et al., 2001; Nony et al., 2003; Boudeau et al., 2003; An et al., 2000). To determine whether GA-mediated decay of PINK1 is also dependent on proteasomal degradation, we blocked proteasome function using two specific inhibitors, epoxomycin and MG132. We found that when COS7 cells expressing PINK1-FLAG were incubated with GA plus either epoxomycin or MG132, but not with other protease inhibitors, degradation of full-length PINK1 was prevented (Fig. 3B). Apparently, upon dissociation of the PINK1–Hsp90 complex, PINK1 is degraded by proteasome.

3.3. Familial PD-associated L347P mutation impairs the interaction between PINK1 and Hsp90/Cdc37

Beilina et al. (2005) recently reported the L347P PINK1 mutant is much more rapidly degraded within cells than wild-type PINK1. To clarify the molecular mechanism underlying the enhanced degradation of the PINK1 mutant, we tested whether PINK1 missense mutants found in familial PD patients (Valente et al., 2004; Hatano et al., 2004) show diminished binding to Hsp90 and/or Cdc37/p50. Immunoprecipitation of PINK1 mutants using anti-FLAG Ab followed by immunoblotting with anti-Hsp90 or Cdc37/p50 Ab revealed that the L347P substitution mutant did not bind to either Hsp90 or Cdc37/p50, whereas the other PD-linked mutations we tested here did not significantly affect the interaction of PINK1 with Hsp90/Cdc37 (Fig. 4A). To confirm the effect of the L347P mutation on protein stability, we also carried out a protein degradation assay and found that the half-life of full-length wild-type PINK1 was 1 h, whereas the half-life of the full-length L347P PINK1 mutant was only 30 min (Fig. 4B). Thus the inability to bind to Hsp90 appears to substantially reduce the stability of the L347P PINK1 mutant.

4. Discussion

Our findings indicate that the molecular chaperone complex Hsp90/Cdc37 bind to PINK1 and thus regulate its stability. Hsp90 is an abundant cytoplasmic protein that functions as a

Please cite this article in press as: Moriwaki, Y., et al., L347P PINK1 mutant that fails to bind to Hsp90/Cdc37 chaperones is rapidly degraded in a proteasome-dependent manner, Neurosci. Res. (2008), doi:10.1016/j.neures.2008.01.006

chaperone and plays an essential role in numerous cellular processes. With fewer target proteins than Hsp60 or Hsp70, Hsp90 appears to primarily bind protein kinases and hormone receptors (Young et al., 2001). To specifically interact with its client proteins, Hsp90 also requires the presence of co-chaperones. One of these, Cdc37/p50, appears to specifically target Hsp90 to a variety of protein kinases, including the mitogen-activated protein kinase (MAPK) family member MAPK-overlapping kinase (MOK) (Miyata et al., 2001), LBK1 (Nony et al., 2003; Boudeau et al., 2003), IKK (Chen et al., 2002) and LRRK2 (Gloeckner et al., 2006). One of the Hsp90/Cdc37 binding proteins IKK was reported to independently bind to both Cdc37 and Hsp90. However, treatment with Hsp90 inhibitors such as GA abolishes the binding ability of IKK to bind both Hsp90 and Cdc37, leading to disruption of its activity. These findings, along with several lines of evidence by the other researchers, suggest that Hsp90 functions in concert with Cdc37 and their interaction is important in their stabilization, activation and/or translocation. Although there is a possibility that Hsp90 and Cdc37 independently bind to PINK1, treatment with Hsp90 inhibitors markedly reduced levels of PINK1 indicate Hsp90/Cdc37 complex are key regulator for PINK1 stability.

Hsp90/Cdc37 interacts with the catalytic domains of several kinases, thereby affecting their enzymatic activity. For example, the interaction of the IKK complex with Hsp90/Cdc37 is required for its activation by tumor necrosis factor (Chen et al., 2002), and the interaction of CDK4 with Hsp90/Cdc37 is required for its proper assembly with cyclin D (Dai et al., 1996). By contrast, the kinase activity of the LKB1 is unaffected by its binding to Hsp90/Cdc37 (Nony et al., 2003). Some recent studies have shown that recombinant PINK1 expressed in *Escherichia coli* has kinase activity (Silvestri et al., 2005; Hatano et al., 2004), but it is not clear whether PINK1 expressed in mammalian cells has similar activity. In our hands, PINK1 exhibited no self-directed phosphorylation activity (data not shown). Further investigation will be required to clarify this issue.

Another function of Hsp90 is stabilization of its target proteins through the prevention of their degradation by the proteasome system. A number of oncogenes, including v-Src (An et al., 2000) and MOK (Miyata et al., 2001), are rapidly degraded in cells following treatment with GA. Consistent with the idea that Hsp90 is a key regulator of PINK1 stability, treatment with Hsp90 inhibitors markedly reduced PINK1 levels within cells (Figs. 2 and 3), while two proteasome inhibitors, epoxomycin and MG132, each prevented Hsp90-inhibitor-induced PINK1 degradation (Fig. 3).

In the present study, we found high concentration of GA treatment conversely augmented PINK1 protein level. Hsp90 was known to form complex with heat shock transcription factor Hsf1, and when this interaction was impaired by adding Hsp90 inhibitor, Hsf1 can form active trimers which enhance the transcription of a subset of genes. According to this idea, other factor(s) induced by Hsf1 may also influence on PINK1 stability.

Beilina et al. (2005) showed that when expressed in either *E. coli* or mammalian cells, steady-state level of the L347P PINK1 mutant is low. They suggested this was the result of enhanced degradation caused by disruption of α-helix similar to that observed in the L166P DJ-1 mutant (Miller et al., 2003). However, we did not observe low steady-state level of L347P PINK1 mutant protein expressed in *E. coli* (data not shown). Instead, the present results suggest that the diminished stability of the L347P PINK1 mutant reflects its inability to interact with Hsp90/Cdc37.

PINK1 reportedly reduces basal neuronal pro-apoptotic activity and protects neurons from staurosporine-induced apoptosis (Silvestri et al., 2005). In addition, Deng et al. (2005) showed that treating cells with PINK1-specific siRNA reduced their viability and significantly increased the cytotoxicity of MPP^+ and rotenone. We found that the L347P mutation diminishes both the interaction of PINK1 with Hsp90 and its stability. These results indicate that L347P mutant PINK1 loses its cell protective function due to destabilization, resulting in the development of PD. Moreover, the present results suggest possible contribution of chaperon system, especially Hsp90, to the pathogenesis of PARK6.

During the preparation of this manuscript, Weihofen et al. (2007) reported that PINK1 interact with Hsp90/Cdc37 complex. They showed GA treatment that affects Hsp90 and client protein interaction preferentially reduced the level of endogenous full-length PINK1. Our findings are consistent with their observations (Figs. 2 and 3). In the present study, we, for the first time, showed that L347P mutant PINK1 displayed diminished interaction with Hsp90/Cdc37, resulting in its instability. Again, these results indicate that L347P mutant PINK1 loses its cell protective function due to destabilization, leading to the development of PD.

Acknowledgements

We thank Dr. Yasuyuki Suzuki for his critical advice and helpful discussions. This study was supported in part by research grants from RIKEN BSI, and a grant-in-aid from the Ministry of Education, Culture, Sports, and Technology of Japan.

References

Abou-Sleiman, P.M., Muqit, M.M., Wood, N.W., 2006. Expanding insights of mitochondrial dysfunction in Parkinson's disease. Nat. Rev. Neurosci. 7, 207–219 review.

An, W.G., Schulte, T.W., Neckers, L.M., 2000. The heat shock protein 90 antagonist geldanamycin alters chaperone association with p210bcr-abl and v-src proteins before their degradation by the proteasome. Cell Growth Differ. 11, 355–360.

Beilina, A., Van Der Brug, M., Ahmad, R., Kesavapany, S., Miller, D.W., Petsko, G.A., Cookson, M.R., 2005. Mutations in PTEN-induced putative kinase 1 associated with recessive parkinsonism have differential effects on protein stability. Proc. Natl. Acad. Sci. U.S.A. 102, 5703–5708.

Boudeau, J., Deak, M., Lawlor, M.A., Morrice, N.A., Alessi, D.R., 2003. Heat-shock protein 90 and Cdc37 interact with LKB1 and regulate its stability. Biochem. J. 370, 849–857.

Chen, G., Cao, P., Goeddel, D.V., 2002. TNF-induced recruitment and activation of the IKK complex require Cdc37 and Hsp90. Mol. Cell 9, 401–410.

Clark, I.E., Dodson, M.W., Jiang, C., Cao, J.H., Huh, J.R., Seol, J.H., Yoo, S.J., Hay, B.A., Guo, M., 2006. Drosophila pink1 is required for mitochondrial function and interacts genetically with parkin. Nature 441, 1162–1166.

Dai, K., Kobayashi, R., Beach, D., 1996. Physical interaction of mammalian CDC37 with CDK4. J. Biol. Chem. 271, 22030–22034.

Dauer, W., Przedborski, S., 2003. Parkinson's disease: mechanisms and models. Neuron 39, 889–909 review.

Deng, H., Jankovic, J., Guo, Y., Xie, W., Le, W., 2005. Small interfering RNA targeting the PINK1 induces apoptosis in dopaminergic cells SH-SY5Y. Biochem. Biophys. Res. Commun. 337, 1133–1138.

Gloeckner, C.J., Kinkl, N., Schumacher, A., Braun, R.J., O'Neill, E., Meitinger, T., Kolch, W., Prokisch, H., Ueffing, M., 2006. The Parkinson disease causing LRRK2 mutation I2020T is associated with increased kinase activity. Hum. Mol. Genet. 15, 223–232.

Hatano, Y., Li, Y., Sato, K., Asakawa, S., Yamamura, Y., Tomiyama, H., Yoshino, H., Asahina, M., Kobayashi, S., Hassin-Baer, S., Lu, C.S., Ng, A.R., Rosales, R.L., Shimizu, N., Toda, T., Mizuno, Y., Hattori, N., 2004. Novel PINK1 mutations in early-onset parkinsonism. Ann. Neurol. 56, 424–427.

Marcu, M.G., Chadli, A., Bouhouche, I., Catelli, M., Neckers, L.M., 2000. The heat shock protein 90 antagonist novobiocin interacts with a previously unrecognized ATP-binding domain in the carboxyl terminus of the chaperone. J. Biol. Chem. 275, 37181–37186.

Miller, D.W., Ahmad, R., Hague, S., Baptista, M.J., Canet-Aviles, R., McLendon, C., Carter, D.M., Zhu, P.P., Stadler, J., Chandran, J., Klinefelter, G.R., Blackstone, C., Cookson, M.R., 2003. L166P mutant DJ-1, causative for recessive Parkinson's disease, is degraded through the ubiquitin-proteasome system. J. Biol. Chem. 278, 36588–36595.

Mineki, R., Taka, H., Fujimura, T., Kikkawa, M., Shindo, N., Murayama, K., 2002. In situ alkylation with acrylamide for identification of cysteinyl residues in proteins during one- and two-dimensional sodium dodecyl sulphate-polyacrylamide gel electrophoresis. Proteomics 2, 1672–1681.

Miyata, Y., Ikawa, Y., Shibuya, M., Nishida, E., 2001. Specific association of a set of molecular chaperones including HSP90 and Cdc37 with MOK, a member of the mitogen-activated protein kinase superfamily. J. Biol. Chem. 276, 21841–21848.

Nakajima, A., Kataoka, K., Hong, M., Sakaguchi, M., Huh, N.H., 2003. BRPK, a novel protein kinase showing increased expression in mouse cancer cell lines with higher metastatic potential. Cancer Lett. 201, 195–201.

Nony, P., Gaude, H., Rossel, M., Fournier, L., Rouault, J.P., Billaud, M., 2003. Stability of the Peutz-Jeghers syndrome kinase LKB1 requires its binding to the molecular chaperones Hsp90/Cdc37. Oncogene 22, 9165–9175.

Park, J., Lee, S.B., Lee, S., Kim, Y., Song, S., Kim, S., Bae, E., Kim, J., Shong, M., Kim, J.M., Chung, J., 2006. Mitochondrial dysfunction in Drosophila PINK1 mutants is complemented by parkin. Nature 441, 1157–1161.

Petit, A., Kawarai, T., Paitel, E., Sanjo, N., Maj, M., Scheid, M., Chen, F., Gu, Y., Hasegawa, H., Salehi-Rad, S., Wang, L., Rogaeva, E., Fraser, P., Robinson, B., St. George-Hyslop, P., Tandon, A., 2005. Wild-type PINK1 prevents basal and induced neuronal apoptosis, a protective effect abrogated by Parkinson disease-related mutations. J. Biol. Chem. 280, 34025–34032.

Silvestri, L., Caputo, V., Bellacchio, E., Atorino, L., Dallapiccola, B., Valente, E.M., Casari, G., 2005. Mitochondrial import and enzymatic activity of PINK1 mutants associated to recessive parkinsonism. Hum. Mol. Genet. 14, 3477–3492.

Unoki, M., Nakamura, Y., 2001. Growth-suppressive effects of BPOZ and EGR2, two genes involved in the PTEN signaling pathway. Oncogene 20, 4457–4465.

Tang, B., Xiong, H., Sun, P., Zhang, Y., Wang, D., Hu, Z., Zhu, Z., Ma, H., Pan, Q., Xia, J.H., Xia, K., Zhang, Z., 2006. Association of PINK1 and DJ-1 confers digenic inheritance of early-onset Parkinson's disease. Hum. Mol. Genet. 15, 1816–1825.

Valente, E.M., Abou-Sleiman, P.M., Caputo, V., Muqit, M.M., Harvey, K., Gispert, S., Ali, Z., Del Turco, D., Bentivoglio, A.R., Healy, D.G., Albanese, A., Nussbaum, R., Gonzalez-Maldonado, R., Deller, T., Salvi, S., Cortelli, P., Gilks, W.P., Latchman, D.S., Harvey, R.J., Dallapiccola, B., Auburger, G., Wood, N.W., 2004. Hereditary early-onset Parkinson's disease caused by mutations in PINK1. Science 304, 1158–1160.

Weihofen, A., Ostaszewski, B., Minami, Y., Selkoe, D.J., 2007. Pink1 Parkinson mutations, the Cdc37/Hsp90 chaperones and Parkin all influence the maturation or subcellular distribution of Pink1. Hum. Mol. Genet. (Epub ahead of print).

Young, J.C., Moarefi, I., Hartl, F.U., 2001. Hsp90: a specialized but essential protein-folding tool. J. Cell Biol. 154, 267–273.

Please cite this article in press as: Moriwaki, Y., et al., L347P PINK1 mutant that fails to bind to Hsp90/Cdc37 chaperones is rapidly degraded in a proteasome-dependent manner, Neurosci. Res. (2008), doi:10.1016/j.neures.2008.01.006

Neurotransmitter release regulated by a MALS–liprin-α presynaptic complex

Olav Olsen,[1] Kimberly A. Moore,[2] Masaki Fukata,[1] Toshinari Kazuta,[1] Jonathan C. Trinidad,[3] Fred W. Kauer,[1] Michel Streuli,[4] Hidemi Misawa,[5] Alma L. Burlingame,[3] Roger A. Nicoll,[1,2] and David S. Bredt[1]

[1]Department of Physiology, [2]Department of Cellular and Molecular Pharmacology, and [3]Department of Pharmaceutical Chemistry, University of California, San Francisco, San Francisco, CA 94143
[4]ImmunoGen, Inc., Cambridge, MA 02139
[5]Department of Neurology, Metropolitan Institute for Neuroscience, Tokyo 183-8526, Japan

Synapses are highly specialized intercellular junctions organized by adhesive and scaffolding molecules that align presynaptic vesicular release with postsynaptic neurotransmitter receptors. The MALS/Veli–CASK–Mint-1 complex of PDZ proteins occurs on both sides of the synapse and has the potential to link transsynaptic adhesion molecules to the cytoskeleton. In this study, we purified the MALS protein complex from brain and found liprin-α as a major component. Liprin proteins organize the presynaptic active zone and regulate neurotransmitter release. Fittingly, mutant mice lacking all three MALS isoforms died perinatally with difficulty breathing and impaired excitatory synaptic transmission. Excitatory postsynaptic currents were dramatically reduced in autaptic cultures from MALS triple knockout mice due to a presynaptic deficit in vesicle cycling. These findings are consistent with a model whereby the MALS–CASK–liprin-α complex recruits components of the synaptic release machinery to adhesive proteins of the active zone.

Introduction

Synaptic transmission requires precise alignment of pre- and postsynaptic specializations. On the presynaptic side, synaptic vesicles containing neurotransmitters must be aligned and docked at active zones, where vesicles fuse with the presynaptic membrane for secretion (Südhof, 2004). On the postsynaptic side, neurotransmitter receptors must be clustered together with relevant signal transduction machinery to respond to released transmitters. Recent studies have begun to elucidate the molecular machinery responsible for the organization of synaptic junctions. Adhesion molecules that span the synaptic cleft function in both stabilization and definition of the presynaptic active zone and postsynaptic specialization (Ichtchenko et al., 1995; Fannon and Colman, 1996; Flanagan and Vanderhaeghen, 1998). Cytosolic molecules associated with these adhesive factors help position synaptic vesicles and neurotransmitter receptors on their respective sides of the synapse (Hata et al., 1996; Torres et al., 1998; Perego et al., 2000).

One such set of modular scaffolding proteins comprises a ternary complex of MALS/Veli (mammalian LIN-7/vertebrate homologue of LIN-7), CASK (peripheral plasma membrane protein), and Mint-1 (munc-18 interacting protein 1), which are vertebrate homologues of a complex first identified in *Caenorhabditis elegans* that mediates vulval development (Kaech et al., 1998). In mammalian brain, the MALS–CASK–Mint-1 complex occurs on both sides of synaptic junctions and is thought to serve distinct roles in these two locations. Presynaptically, this complex links to neurexin (Hata et al., 1996), an adhesion molecule that binds across the synapse to postsynaptic neuroligin (Ichtchenko et al., 1995). Furthermore, Mint-1 associates with Munc18-1, an essential component of the synaptic vesicle fusion machinery (Okamoto and Südhof, 1997). Postsynaptically, MALS binds to the *N*-methyl-D-aspartate (NMDA)–type of glutamate receptors (Jo et al., 1999) and is reported to transport NMDA receptor vesicles along microtubules (Setou et al., 2000).

Genetic studies have failed to establish the essential roles of the MALS–CASK–Mint-1 complex in brain. Three MALS genes exist in mammals (Borg et al., 1998; Butz et al., 1998; Jo et al., 1999), and targeted disruption of MALS-1 and MALS-2 leads to compensatory up-regulation of MALS-3 in the CNS (Misawa et al., 2001). Mint-1 mutant mice show no defects in

Correspondence to David S. Bredt: bredt@itsa.ucsf.edu

Abbreviations used in this paper: AMPA, α-amino-3-hydroxy-5-methyl-4-isoxazolepropionate; CaMK, CAM kinase; DIV, days in vitro; EPSC, excitatory postsynaptic current; MS, mass spectrometry; NMDA, *N*-methyl-D-aspartate; PSD, postsynaptic density; SAM, sterile α motif; TKO, triple knockout; WT, wild type.

The online version of this article contains supplemental material.

© The Rockefeller University Press $8.00
The Journal of Cell Biology, Vol. 170, No. 7, September 26, 2005 1127–1134
http://www.jcb.org/cgi/doi/10.1083/jcb.200503011

Supplemental Material can be found at:
http://www.jcb.org/cgi/content/full/jcb.200503011/DC1

excitatory synaptic transmission and only a subtle defect in inhibitory synaptic transmission (Ho et al., 2003). Also, no synaptic analysis has been reported for CASK knockouts that die at birth due to midline defects (Laverty and Wilson, 1998).

Several molecules that mediate synapse development have been identified through invertebrate genetic studies. For example, mutation of *C. elegans syd-2* disperses presynaptic active zones (Zhen and Jin, 1999). A similar structural defect occurs in flies lacking the *Drosophila melanogaster syd* orthologue liprin-α, which exhibits a concomitant decrease in synaptic transmission (Kaufmann et al., 2002). Liprin-α binds to a receptor protein tyrosine phosphatase, Dlar (Serra-Pages et al., 1998), suggesting a model whereby liprin-α and Dlar cooperate to organize presynaptic active zones. How liprin-α links to the synaptic vesicle machinery remains uncertain.

To define the essential roles for the MALS complex in mammals, we purified the MALS complex from brain. Isolation of the MALS complex revealed an association with a family of cytoskeletal and presynaptic adhesion molecules. Importantly, we found liprin-α1, -α2, -α3, and -α4 in the MALS complex. Association with this complex is mediated through the SAM domains in liprin-α and an NH_2-terminal region in CASK. Using the sterile α motif (SAM) domains of liprin-α as a dominant negative, we disrupted the MALS–liprin complex in dissociated neurons. To understand the function of the MALS complex, we generated mutant mice lacking all three MALS genes. Mice lacking any single gene were viable and fertile. However, mice lacking all three MALS genes died within one hour of birth. This perinatal lethality is associated with impaired presynaptic function, reflecting the presynaptic deficits of invertebrates lacking liprin-α orthologues. These studies establish a crucial role for the MALS complex in synaptic vesicle exocytosis and implicate liprin-α in this process.

Results

Proteomic characterization of the MALS complex in brain

To identify molecular roles for MALS, we assessed the composition of the MALS protein complex. We performed preparative immunoprecipitation of MALS-3 from brain homogenates and used MALS-3 knockout mice (Fig. S1, available at http://www.jcb.org/cgi/content/full/jcb.200503011/DC1) as a powerful control. A series of protein bands were present in the MALS-3 immunoprecipitation that were absent in precipitations from MALS-3 knockouts. Several known components of the MALS-3 complex were identified, including neurexin, CASKIN, NMDA receptor 2B, Mint-1, and PALS-1, which is a protein associated with lin-7 (Fig. 1 A). Silver staining of immunoprecipitates showed specific bands at 140, 120, and 105 kD (Fig. 1 A). Mass spectrometry indicated that the 105-kD band corresponds to CASK, the 120-kD band corresponds to SAP-97, and the 140-kD band contained Mint-1, as well as liprin-α2, -α3, and -α4 (Fig. 1 A). Western blotting confirmed the efficient coimmunoprecipitation of CASK, Mint-1, and liprin-α1 and -α2 (Fig. 1 B).

Interaction of liprin-α with the MALS complex

Liprin-α mutants in *D. melanogaster* (and *syd* mutants in *C. elegans*) display impaired synaptic vesicle exocytosis. Our discovery that liprin-α binds to the MALS–CASK complex is novel. Consistent with this, MALS, CASK, and liprin-α2 were enriched in synaptic biochemical fractionations of brain extracts (Fig. 1 C). Furthermore, MALS partially colocalized with liprin-α2 and the presynaptic marker synaptophysin in cultured hippocampal neurons (Fig. 1, D and E).

Liprin-α proteins contain conserved coiled-coil regions, three SAM domains, and a COOH-terminal region that binds to

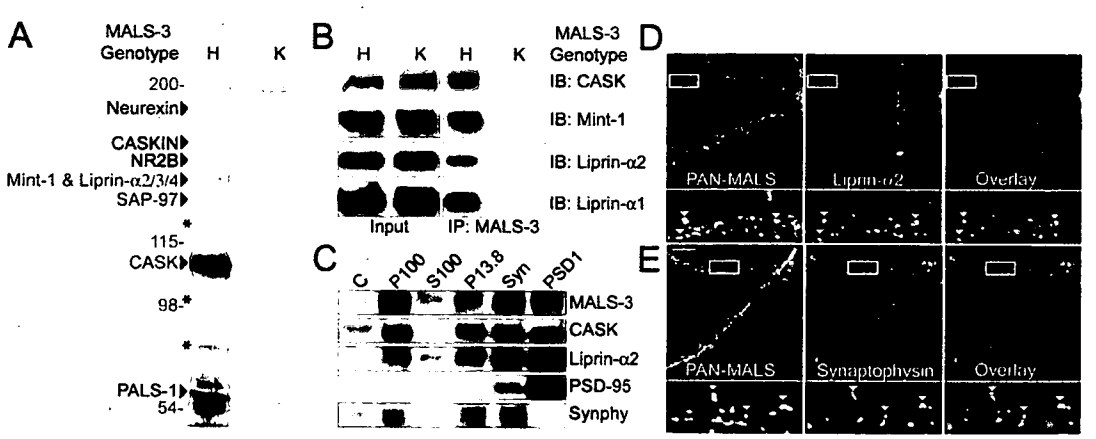

Figure 1. **Identification of a neuronal protein complex containing MALS and liprin-α.** (A) Immunoprecipitation of MALS-3 from brain extracts showed a series of bands in heterozygote (H) that were absent from MALS-3 knockout (K). Bands were identified by MS/MS obtained using a micro-ionspray source attached to a mass spectrometer (red) and confirmed by Western blotting (black). Molecular weights are presented in blue and Mint-1 degradation products are shown with asterisks. (B) Western blotting of heterozygote and knockout brain extracts immunoprecipitated for MALS-3 shows specific association of CASK, Mint-1, liprin-α1, and -α2 with MALS-3. (C) Western blotting shows that MALS-3, CASK, and liprin-α2 are highly enriched with synaptophysin (Synphy) in the synaptosome (Syn) fraction and PSD-95 in PSD fractions. (D and E) Hippocampal cultures (28 DIV) were stained for MALS, liprin-α2, and synaptophysin. Immunostaining reveals that both liprin-α2 (D) and synaptophysin (E) partially colocalize with MALS (arrowheads). Bar, 20 μm.

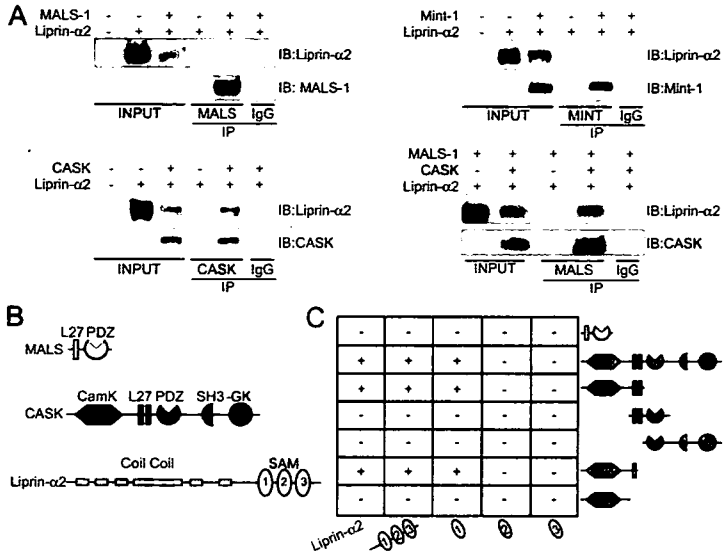

Figure 2. **Domain mapping of the MALS–liprin-α interaction.** (A) CASK, but not MALS-1 or Mint-1, coimmunoprecipitated liprin-α2 in transfected COS cells. In the presence of CASK, MALS coimmunoprecipitated liprin-α2. (B) Schematics representing the structural domains of MALS-3 (blue), CASK (orange), and liprin-α2 (yellow). (C) By yeast two-hybrid analysis, CASK, but not MALS-3, interacted with liprin-α2. For CASK–liprin-α binding, the SAM1 domain of liprin-α2 is sufficient for interaction with CASK. Both the CaMK-like domain and first L27 domain of CASK were necessary for binding to liprin-α2.

certain PDZ domains (Fig. 2 B). Using immunoprecipitation analysis and the yeast two-hybrid system, we found that MALS-1 does not directly bind to liprin-α2 (Fig. 2, A [top left] and C). We therefore asked whether other core components of the MALS complex might directly associate with liprin-α2. Indeed, CASK, but not Mint-1, bound to liprin-α2 directly (Fig. 2 A, bottom left and top right). Furthermore, we found that CASK can link liprin-α2 to a MALS-1 complex (Fig. 2 A, bottom right). These biochemical associations also redirect protein distribution in transfected cells, and all three MALS isoforms can associate with CASK to form MALS–CASK–liprin-α complexes (Figs. 1 and 2; unpublished data).

To define the site for interaction between liprin-α2 and CASK, we used the yeast two-hybrid system. We found that full-length CASK readily bound to full-length liprin-α2 (Fig. 2 C). This binding was mediated specifically by the first SAM domain in liprin-α2. Deletion analysis of CASK showed that the CAM kinase (CaMK) and first L27 domain of CASK were necessary for binding. We were unable to map this interaction further, suggesting that the binding domain may require large sequences for proper folding.

Targeted disruption of MALS-3 and breeding of MALS-deficient mice

To examine the essential roles for MALS in this complex, we targeted disruption of MALS-3. Our targeting vector replaced exons 3, 4, and 5 of MALS-3 with a neomycin cassette (Fig. S1, A–C). After targeted disruption in embryonic stem cells, we generated MALS-3–deficient mice. MALS-3 mutant mice were born at the expected Mendelian ratios and displayed no overt behavioral abnormalities. Western blotting showed a complete absence of MALS-3 protein in the knockout (Fig. S1 D). Histological inspection of brain showed no gross anatomical abnormalities. As previously reported (Misawa et al., 2001), MALS-3 occurs diffusely in numerous neuronal populations in the brain (Fig. S1 E). Furthermore, expression of MALS-3 is up-regulated, especially in the dentate gyrus region of the hippocampus, in MALS-1/2 double knockout mice (Fig. S1 E).

We interbred MALS-3 knockout mice with the previously generated MALS-1/2 mutants, which yielded 27 possible genotypes. These compound genotypes are presented in Fig. 3 A. We found that most mice lacking both MALS-1 and -3 died shortly after birth, whereas mice lacking MALS-1 and -2 were viable and fertile. Mice lacking MALS-2 and -3 and heterozygous for MALS-1 died during the second postnatal week. Finally, mice lacking all three MALS isoforms exhibited irregular, labored breathing and died within one hour of birth. The complete absence of MALS is not associated with embryonic lethality, as the predicted Mendelian ratio of fetuses was found when a caesarian section was performed at embryonic day 18 (Fig. 3 B).

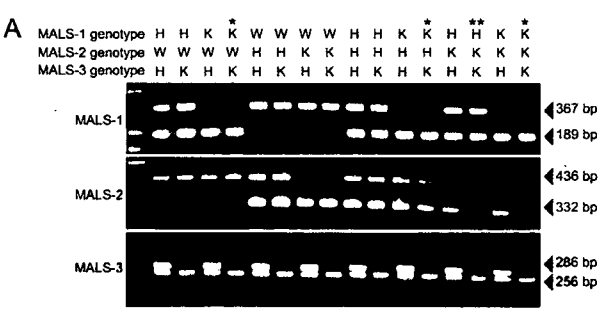

B

	2 wk postnatal			Embryonic d 17/18		
MALS-1 genotype	K	K	K	K	K	K
MALS-2 genotype	K	K	K	K	K	K
MALS-3 genotype	W	H	K	W	H	K
Observed Number	74	145	0	23	53	27
Observed Ratio	1	1.96	0	1	2.3	1.1
Expected Ratio	1	2	1	1	2	1

Figure 3. **Generation of mice lacking all three MALS isoforms.** (A) PCR genotyping of MALS mice. Single asterisk indicates mice that died within hours of birth and double asterisk indicates a line that died in their second postnatal week. (B) Statistics obtained from crossing MALS-1/2 K and MALS-3 H mice. Genotyping 2-wk-old mice showed no TKO mice. However, embryonic mice (E18) showed the predicted ratio of W, H, and K mice.

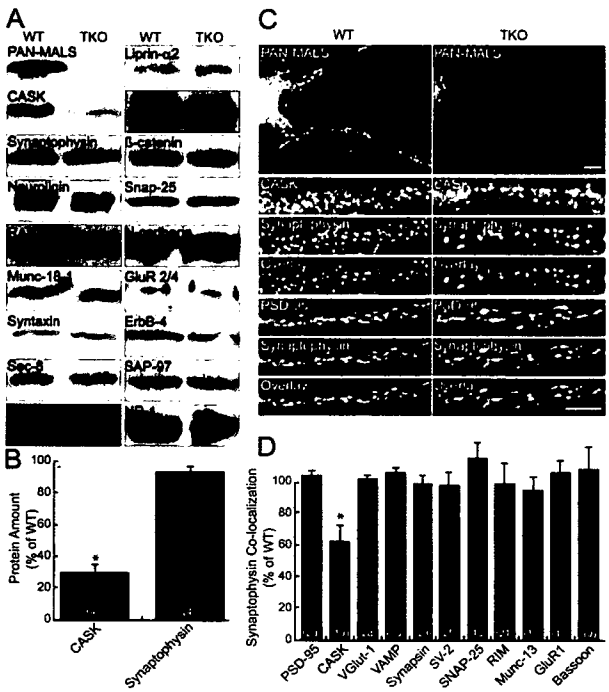

Figure 4. **CASK expression is reduced in MALS-deficient mice.** (A) Brains from E18 mice were immunoblotted for numerous synaptic proteins. (B) CASK was markedly reduced (31% of control ± 8; *, $P < 0.01$) in the TKOs, but no changes in other synaptic proteins were detected. (C and D) Similarly, cultured hippocampal neurons lacking MALS displayed normal localization of several pre- and postsynaptic markers but showed reduced colocalization of CASK (red) and synaptophysin (green), suggesting that CASK is partially lost from synapses (62% ± 12 of control; *, $P < 0.01$). Bars: (top) 10 μm; (bottom) 5 μm. All error bars represent SEM.

Disruption of the MALS-CASK-liprin-α complex

MALS triple knockout (TKO) mice appear anatomically normal at birth; however, their perinatal death and difficulty breathing suggest neurological deficits. To assess whether components of the MALS complex or other synaptic proteins show quantitative expression differences, we performed Western blotting in the MALS TKO mice as compared with MALS-1/2 knockout mice, which were phenotypically normal, or wild type (WT). We found that CASK levels are dramatically decreased in the MALS TKO, whereas levels of all other assayed synaptic proteins were normal in the TKO mice (Fig. 4, A and B). We also found that the synaptic localization of CASK, but not other synaptic markers, was partially disrupted in TKO neuronal cultures (Fig. 4, C and D).

Liprins play important roles in synaptic development and function. Because we did not detect any change in liprin-α amount or localization (unpublished data), we suspected that the MALS–CASK complex may be a downstream effector for liprin-α's presynaptic function. To test this hypothesis, we generated dominant-negative liprin-α constructs consisting of the SAM domains fused to GFP in the PSCA1 Semliki Forest viral vector to disrupt the liprin-α–CASK interaction. Infection of neurons with Semliki virus expressing GFP alone showed that >90% of neurons were infected and that neither the virus nor GFP affected MALS distribution (Fig. 5 A). However, expression of the liprin dominant-negative (GFP-SAM) misdirected MALS to nonsynaptic sites and significantly disrupted synaptic localization of MALS (Fig. 5 B). These results suggest that liprin-αs are upstream of MALS and may function, at least partially, through their interaction with the MALS–CASK complex.

MALS-deficient mice have deficient neurotransmitter release

Because of the perinatal death of MALS TKO mice, we were unable to assess electrophysiological parameters in forebrain neurons. Therefore, we generated microisland neuronal cultures from these mice to assess synaptic function. Individual neurons in such cultures are grown on isolated dots of substrate and form functional autaptic synapses. Because liprin-αs are necessary for proper synapse differentiation, we examined the morphology and number of synapses in autapses from TKO mice. We found that neurons from MALS TKO formed autaptic synapses in which presynaptic synaptophysin was juxtaposed to postsynaptic density (PSD)-95 (Fig. 6 A). The density of synapses in the TKO was comparable to WT (Fig. 6 B);

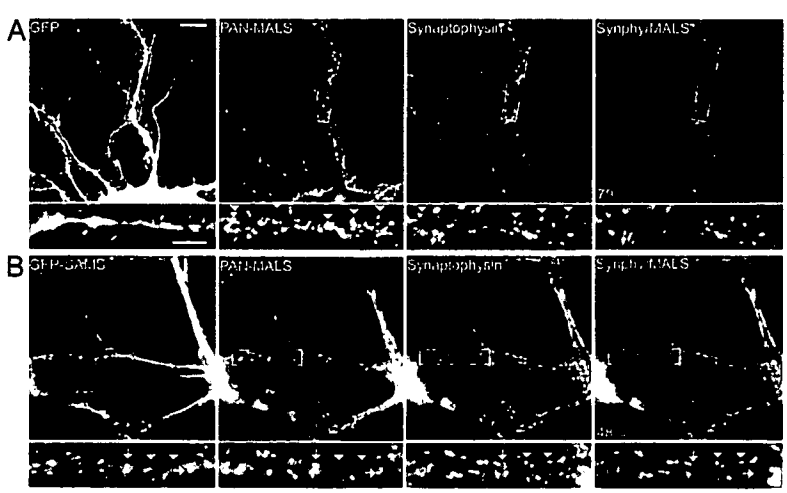

Figure 5. **A dominant-negative liprin-α disrupts presynaptic localization of MALS.** Hippocampal cultures (35 DIV) were infected with Semliki Forest virus expressing either GFP or GFP fused to the SAM domains of liprin-α2. Whereas infection and expression of GFP had no effect on synaptic expression of MALS (A, arrowheads), expression of the dominant-negative (GFP-SAM) construct misdirected MALS to nonsynaptic sites (B, arrows) and resulted in a loss of presynaptic MALS (B, arrowheads). Quantification of immunofluorescence reveals that colocalization of MALS (red in overlayed images) with synaptophysin (green in overlayed images) is significantly reduced in neurons expressing GFP-SAM, from 77.3% ± 3.6 in uninfected neurons to 48.1% ± 2.1 and to 79.5% ± 2.0 in GFP-expressing neurons ($P < 0.01$). Bars: (top) 20 μm; (bottom) 10 μm.

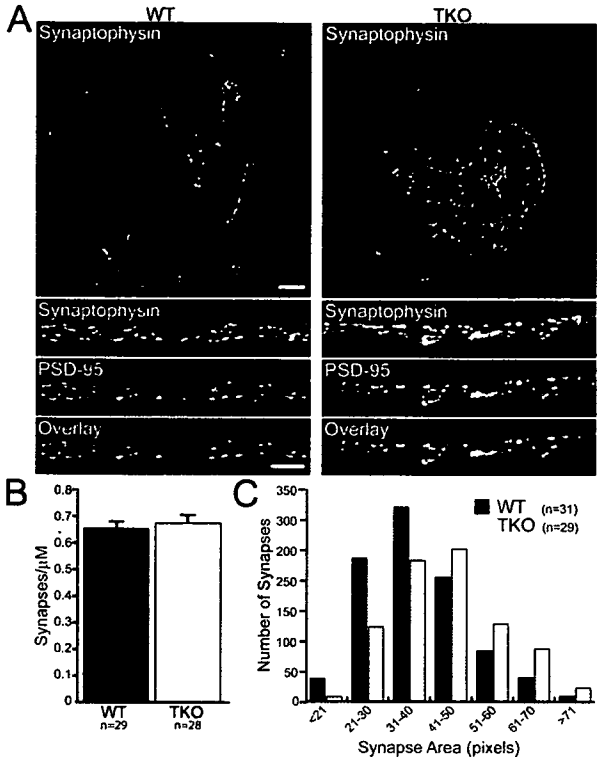

Figure 6. **Synapse size, but not number, is altered in neurons lacking MALS.** Autaptic cultures (14 DIV) from control and TKO mice were stained with antibodies to PSD-95 and synaptophysin. (A) Representative autaptic neurons from WT and TKO mice stained with synaptophysin. Bars: (top) 20 μm; (bottom) 5 μm. (B) PSD-95/synaptophysin staining revealed that the number of synapses was unaltered in TKO cultures (0.65 ± 0.15 and 0.67 ± 0.18 synapses/μm for WT and TKO, respectively). (C) As determined by synaptophysin staining, the distribution of presynaptic terminal size was shifted to the right in the TKO ($P < 0.01$). All error bars represent SEM.

however, the distribution of synaptic areas in the TKO was shifted to slightly larger sizes (Fig. 6 C).

Electrophysiological experiments demonstrated that excitatory postsynaptic currents (EPSCs) in the MALS TKO cultures were profoundly reduced relative to WT (Fig. 7 A). Furthermore, the rate and degree of EPSC depression during high frequency stimulation (10 Hz) was enhanced in the MALS TKO autapses (Fig. 7 B), suggesting that the MALS–liprin-α complex plays a role in presynaptic vesicle cycling. Because MALS mutant mice die around birth, structural analyses of mature synapses are not feasible. However, the magnitude and distribution of miniature EPSCs was comparable in MALS TKO and WT cultures (Fig. 7 C), arguing against a postsynaptic defect. Indeed, the ratio of the α-amino-3-hydroxy-5-methyl-4-isoxazolepropionate (AMPA)/NMDA components of the EPSC was normal (Fig. 7 D), suggesting that trafficking and clustering of these receptors are intact.

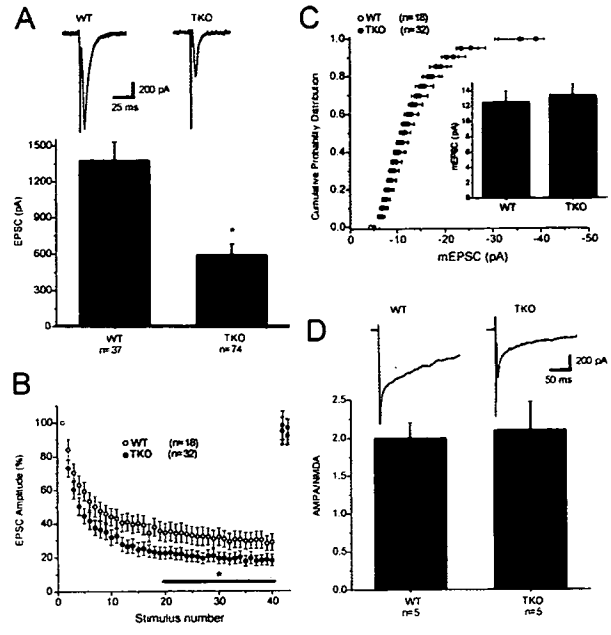

Figure 7. **Neurons from MALS-deficient mice display abnormal synaptic transmission.** (A) EPSCs recorded in autaptic cultures prepared from E18 MALS TKO mice were profoundly reduced relative to EPSCs recorded in WT cultures (*, $P = 0.01$). Typical EPSCs recorded in WT and MALS TKO pyramidal cell autapses are shown above. (B) Normalized synaptic responses during a 10-Hz (4 s) stimulus train. Decay of EPSCs during the high frequency train was greater in the MALS TKO autapses than in WT autapses (*, $P < 0.05$). EPSCs returned to baseline values within 5 s of the end of the stimulus train in both populations ($n = 18$ and 7 for WT and MALS TKO, respectively, for the recovery). (C) The distribution and amplitude of miniature EPSCs was the same in autapses prepared from WT and MALS TKO mice ($P > 0.1$). (D) The ratio of AMPA EPSCs to NMDA EPSCs was also similar in WT and MALS TKO autapses ($P > 0.1$). AMPA EPSCs were measured at the peak (~8–10 ms after the action potential), whereas NMDA EPSCs were measured at 40 ms after the action potential, a time point when the AMPA EPSC has decayed to baseline. Typical AMPA/NMDA EPSCs from the two populations are shown. All error bars represent SEM.

Discussion

MALS proteins are essential

This study establishes MALS as an essential protein family involved in neurotransmitter release. MALS are components of a large presynaptic protein complex that includes scaffolding proteins, adaptor proteins, and adhesion molecules (Butz et al., 1998). Importantly, we find that liprin-α isoforms are components of this complex. Because liprin-α orthologues define the dimensions of the active zone in invertebrate synapses (Zhen and Jin, 1999; Kaufmann et al., 2002), the MALS complex has the potential to link adhesion molecules to the exocytotic machinery.

Although each strain of individual MALS knockouts is viable and fertile, certain combinations are synthetically lethal. Mice lacking all three MALS isoforms die within one hour of birth and have a severe breathing defect. This defect resembles the phenotype of mice lacking all three neurexin isoforms (Missler et al., 2003), which are also part of the MALS complex (Hata et al., 1996). Previous studies showed that MALS can bind to the COOH termini of proteins typical for morphological development, including β-catenin and epidermal growth factor receptors (Garcia et al., 2000; Perego et al., 2000; Shelly et al., 2003). That MALS TKO mice show no gross external abnormalities suggests that MALS does not play general

roles in tissue morphogenesis. Detailed histological evaluation may, however, reveal specific tissues whose development requires the MALS complex.

Presynaptic defect in MALS mutants

The perinatal lethality and labored breathing of MALS TKO are phenotypes often seen in mice with impaired synaptic transmission. Consistent with this, we found a profound presynaptic defect in these mutants. No change in the mEPSC amplitude distribution and no change in the ratio of AMPA/NMDA receptor–mediated currents were observed. In contrast to normal postsynaptic function, high-frequency stimulation produced an accelerated and more pronounced synaptic depression, suggesting greater depletion of vesicles in the readily releasable pool of MALS TKO mice. These results also imply that the MALS–CASK–liprin-α complex helps determine the size of the releasable pool and is important for replenishing this pool from the reserve pool.

Assembly of the MALS protein complex

The presynaptic defects in MALS TKO mice are paralleled by the association of MALS with a large presynaptic complex. Numerous modular protein interaction interfaces assemble this complex. The membrane-associated guanylate kinase CASK directly binds to many components and therefore constitutes the core. MALS uses its coiled-coil L27 domain to bind to the second of two L27 domains in CASK (Lee et al., 2002). The first L27 domain in CASK associates with the NH_2-terminal L27 domain of SAP-97 (Lee et al., 2002). Neurexin binds to the PDZ domain of CASK (Hata et al., 1996) and Mint-1 binds to the CaMK domain of CASK (Butz et al., 1998; Borg et al., 1999). Furthermore, we find that liprin-α proteins associate with the NH_2-terminal region of CASK, which includes the CaMK domain and the first L27 region. Previous studies showed that liprin-α proteins also bind to LAR-family receptor protein tyrosine phosphatase (Serra-Pages et al., 1998) and to the Rab3A binding protein RIM1α (Schoch et al., 2002). Our failure to detect LAR or RIM proteins in the MALS complex may suggest that interaction of CASK with the SAM domains of liprin-α occludes association with these other presynaptic molecules.

The liprin protein family comprises seven liprin isoforms that are subdivided into the α- and β-type. We identified only liprin-α family members as part of the MALS complex. The SAM1 domain of liprin-αs mediates their interaction with CASK. These domains are highly conserved between liprin-α proteins, sharing >90% identity. In contrast, liprin-α SAM1 domains share <45% identity with the most homologous liprin-β member. The SAM1 domain of liprin-α is evolutionarily conserved; mammalian liprin-αs share >90% identity with orthologues in *D. melanogaster* and *C. elegans*, which suggest that the liprin-α–CASK interaction is likely conserved.

Potential mechanisms for MALS complex regulating transmitter release

Our discovery that the MALS complex contains liprin-α proteins can explain how this complex participates in synaptic vesicle exocytosis. Genetic analysis of invertebrates shows that liprin-α in *D. melanogaster* and its homologue *syd* in *C. elegans* control presynaptic function and morphology (Zhen and Jin, 1999; Kaufmann et al., 2002). In addition to these developmental defects, these mutants show decreased synaptic transmission resembling that seen in the MALS TKO. Because the mammalian genome contains four liprin-α isoforms (Serra-Pages et al., 1998), functional analyses are difficult. Some biochemical work suggests that mammalian liprin-α proteins may be postsynaptic and regulate AMPA receptors through the glutamate receptor interacting protein GRIP (Wyszynski et al., 2002). *lin-10* also has been shown to regulate GLR-1 in *C. elegans* (Rongo et al., 1998). MALS and liprin-αs are also enriched in PSD fractions from rat brain (Fig. 1 C) and partially colocalize with PSD-95 in cultured hippocampal neurons (Fig. S2, available at http://www.jcb.org/cgi/content/full/jcb.200503011/DC1). We cannot rule out the possibility that postsynaptic MALS may contribute to the synaptic defect in the MALS TKOs, but our failure to detect GRIP or AMPA receptors in the MALS complex suggests no role for postsynaptic liprin-α in our analysis. Because MALS mutant mice die around birth, conditional mutants of the MALS may be required to evaluate roles for this complex in synaptic morphogenesis.

This study provides the first evidence that the MALS complex plays an important role in controlling transmitter release at excitatory synapses in brain. The myriad of interactions for the core MALS–CASK complex has suggested diverse roles; however, decisive genetic evidence has been lacking. Our work is consistent with a model whereby this complex recruits components of the synaptic release machinery to adhesive proteins of the active zone. According to this proposal, the MALS–CASK complex would couple extracellular synaptic interactions to the intercellular organization of the presynaptic secretory machinery.

Materials and methods

Antibodies

Isoform-specific and pan antibodies against MALS-1, -2, and -3 were generated in rabbits as described previously (Misawa et al., 2001). Mouse anti–liprin-α1 (C3-77) and -α2 (245:2:1) antibodies have also been described previously (Serra-Pages et al., 1998). Mouse anti-CASK, MINT, ZO-2, Sec8, β-catenin, and N-cadherin were all purchased from Transduction Labs. Munc-18, Rab5, and neuroligin antibodies were purchased from Synaptic Systems GmbH. Rabbit anti-CASK and antisynaptophysin were obtained from Zymed Laboratories. The mouse anti–Erb-B4 antibody was purchased from Lab Vision/Neomarkers and anti–PSD-95 antibody was obtained from Affinity BioReagents, Inc. The mouse anti-GluR 2/4 antibody was purchased from Chemicon International and rabbit synaptophysin was obtained from Sigma-Aldrich.

Immunoprecipitations

Using a Potter homogenizer (Braun), adult mouse brains from either MALS-3 heterozygote or knockout mice were homogenized in three volumes of STE buffer (320 mM sucrose, 20 mM Tris, pH 8.0, and 2 mM EDTA) containing 10 μg/ml leupeptin and 200 μg/ml PMSF. Homogenates were spun at 20,000 *g* for 1 h and pellets were resuspended in TET buffer (20 mM Tris, pH 8.0, 1 mM EDTA, and 1.3% Triton X-100) containing 10 μg/ml leupeptin and 50 μg/ml PMSF. After rehomogenization with a Potter homogenizer and a 1-h incubation at 4°C, the lysates were spun at 100,000 *g* for 1 h. The supernatant was collected and precleared with protein A–Sepharose (GE Healthcare) for 1 h at 4°C. Precleared lysates were immunoprecipitated with 10 μg MALS-3 antibody or control rabbit IgG for 2 h at 4°C. To collect immunoprecipitated protein complexes,

80 μl of a 50% protein A–Sepharose slurry was added to the lysates and incubated for 1 h at 4°C. Immunoprecipitates were washed extensively and loaded onto SDS-PAGE to separate the proteins. Gels were either silver stained or transferred to nitrocellulose for Western blotting. Immunoprecipitations from COS cells were performed similarly, except that the cells were directly lysed in TET buffer and spun at 20,000 *g* for 10 min, and supernatants were collected.

Immunocytochemistry

Hippocampal cultures grown on poly-D-lysine–treated coverslips were fixed with 4% PFA on ice for 10 min followed by methanol at −20°C. After thorough washing with PBS containing 0.1% Triton X-100 (PBS-X), cells were blocked with PBS-X containing 3% normal goat serum (blocking solution). Primary antibodies were incubated for 2 h at RT or 4°C overnight in blocking solution. Cells were washed three times with PBS-X and incubated with secondary antibodies in blocking solution for 1 h at RT. Cells were washed with PBS-X and mounted onto slides with Fluoromount-G (Southern Biotechnology Associates, Inc.).

Colocalization experiments in neurons were performed using images acquired from a confocal microscope (model LSM510; Carl Zeiss MicroImaging, Inc.) and analyzed using image analysis software (MetaMorph). Neurons were chosen randomly for quantification. For all images, thresholds were set at a predetermined level and colocalization values were obtained using MetaMorph software. Statistical significance was determined by an unpaired *t* test.

Nano-LC-ESI-Qq-TOF tandem mass spectrometry (MS) analysis

Individual gel bands were reduced with 10 mM dithiothreitol at 56°C for 1 h followed by alkylation with 55 mM iodoacetamide for 45 min at RT. The proteins were digested overnight with 12 ng/μL trypsin at 37°C. Peptides were extracted with a 50% acetonitrile/5% formic acid solution. The peptides were dried down and resuspended in 0.1% formic acid, and then separated via HPLC using a 75 μM × 15 cm reverse phase C-18 column (LC Packings) at a flow rate of 350 nl/min running a 3–32% acetonitrile gradient in 0.1% formic acid on an 1100 series HPLC (Agilent Technologies). The LC eluent was coupled to a micro-ionspray source attached to a mass spectrometer (model QSTAR Pulsar; MDS Sciex). Peptides were analyzed in positive ion mode. MS spectra were acquired for 1 s, followed by 3-s MS/MS on the most intense multiply charged peak.

Subcellular fractionation

Subcellular fractions of rat brain were prepared by differential centrifugation. Brains were homogenized in buffer containing 320 mM sucrose and 10 mM Hepes-NaOH, pH 7.4. Homogenate (C, crude lysate) was centrifuged for 10 min at 1,000 *g* to produce a pellet. The supernatant was centrifuged at 13,800 *g* for 10 min to produce a pellet (P13.8) and supernatant. The pellet was resuspended in the original volume of homogenization buffer and centrifuged at 100,000 *g* to yield a pellet (P100, crude synaptosomal vesicle pellet) and supernatant (S100, crude cytosolic synaptosomal supernatant). Synaptosome and PSD fractions were isolated by a discontinuous sucrose gradient centrifugation using P13.8. The pellet was extracted twice with ice cold 0.5% Triton X-100 (synaptosome) and then centrifuged to obtain the PSD pellet.

Cell culture and transfections

Hippocampal cultures were prepared as described previously (Tomita et al., 2003). In brief, hippocampi were dissected from 17- and 18-d-old embryos, digested with papain solution and plated at a density of 5×10^4 neurons/well in 24-well dishes. Neurons were cultured in Neurobasal media (GIBCO BRL) supplemented with B27, penicillin, streptomycin, and L-glutamine according to the manufacturer's protocol (GIBCO BRL). COS cells were grown in DME supplemented with 10% FBS, 100 U/ml penicillin, and 100 μg/ml streptomycin. Transfections were performed using LipofectAMINE Plus (Invitrogen) according to the manufacturer's protocols. Transfected cells were used for immunocytochemistry or immunoprecipitations 48 h after the transfection of plasmids.

Constructs

pcDNA3 MALS-1, -2, and -3 and HA-liprin-α2 constructs have been described previously (Serra-Pages et al., 1998; Misawa et al., 2001). For construction of EGFP-MALS and CASK, full-length clones were amplified by PCR and cloned downstream of EGFP. For construction of yeast two-hybrid clones, liprin-α2 constructs were amplified by PCR and cloned into the pGBKT7 vector. Liprin-α2 constructs were as follows: full-length (aa 2–1257), SAMS 1/2/3 (aa 705–1257), SAM 1 (aa 876–984), SAM 2 (aa 997–1105), and SAM 3 (aa 1086–1197). MALS and CASK clones were amplified and cloned into the pGADT7 vector as follows: full-length MALS-1 (aa 2–233), full-length CASK (aa 2–909), CASK STK/L27AB (aa 2–476), CASK L27/PDZ (aa 276–590), CASK PDZ/SH3GK (aa 476–909), CASK STK/L27A (aa 2–405), and CASK STK (aa 2–346). Viral constructs were subcloned from pGBKT7 into a modified pBK-CMV plasmid to produce an NH_2-terminal GFP-fusion and then subcloned into PSCA1 plasmid.

Yeast two-hybrid

Yeast cotransformation was performed according to the manufacturer's protocol (CLONTECH Laboratories, Inc.) with the yeast strain AH109. Binding was assessed by quantification of colonies transformed with the indicated plasmids on –LWH plates. Interactions were scored as positive (+) if many (>50) individual colonies were observed or negative (−) if no colonies were present on the –LWH plate. Control plates (–LW) were used to verify transformation efficiency.

Isolation of MALS-3 genomic DNA and construction of targeting vector

A mouse MALS-3 cDNA probe was used to isolate bacterial artificial chromosome clones from a 129Sv/J mouse genomic library (Genome Systems, Inc.). The targeting vector was constructed using the pPNT replacement vector. A 1-kb region downstream from the targeted exons was PCR-amplified, digested with XhoI and NotI, and subcloned into the XhoI–NotI sites of pPNT. Similarly, a 5-kb genomic region upstream from the targeted exons was PCR-amplified, digested with BamHI and XbaI, and inserted into the BamHI–XbaI sites of the pPNT vector. In the targeting vector, the third, fourth, and fifth exons (as well as the third and fourth introns of MALS-3) were replaced with a neocassette.

Generation of MALS-3 null mice

The targeting vector was linearized with BamHI and electroporated into R-1 embryonic stem cells. Clones resistant to G418 and gancyclovir were analyzed for recombination by PCR. To ensure proper homologous recombination, PCR-positive clones were further analyzed by Southern blotting using probes containing genomic sequences outside of the targeting vector and with a neoprobe. Properly targeted clones were injected into blastocysts from C57BL6 (The Jackson Laboratory) mice and transferred to surrogate mothers. Male chimeras were mated with C57BL6 females for transmission of the mutated allele through the germ line. Heterozygous mice were interbred to generate MALS-3 null mice. The genotypes from these and subsequent matings were determined by Southern blotting or PCR using allele-specific primers as follows: GGAAGAAATGGAGTCCCGCTTTG and ACAGCAGGACAGAACTGTCC for the WT allele; GCTAAAGCGCATGCTCCAGACTG and ACAGCAGGACAGAACTGTCC for the targeted allele. The null phenotype was confirmed by Western blotting of brain homogenates with antibodies to MALS-3.

Generation of MALS TKO mice

Female MALS-1/2 null mice (Misawa et al., 2001) and male MALS-3 null mice were mated, generating MALS-1/2/3 triple heterozygous mice. Triple heterozygous mice were bred back to MALS-1/2 null mice, and MALS-1/2 double null and 3 heterozygous mice were selected. These mice were interbred to generate MALS-1/2/3 triple null mice. Genotyping for the MALS-1 and -2 targeted loci has been described previously (Misawa et al., 2001).

Electrophysiology

Microdot cultures were prepared as described previously (Bekkers and Stevens, 1991; Augustin et al., 1999). For whole cell voltage-clamp recordings in autaptic culture (10–18 days in vitro [DIV]), patch pipette solutions contained the following: 135 mM potassium gluconate, 10 mM Hepes, 1 mM EGTA, 4.6 mM $MgCl_2$, 4 mM NaATP, 15 mM creatine phosphate, 50 U/ml phosphocreatine kinase, pH 7.3, and 300 mM mOsm. The extracellular solution contained 140 mM NaCl, 2.4 mM KCl, 10 mM Hepes, 10 mM glucose, 4 mM $CaCl_2$, 4 mM $MgCl_2$, pH 7.3, and 300 mM mOsm. To determine the ratio of AMPA/NMDA EPSCs, $MgCl_2$ was omitted from the extracellular solution; the patch pipette and extracellular solutions were prepared as previously described (Tovar and Westbrook, 1999). Cells were held at −70 mV and stimulated at 0.1 Hz with a 1–4 ms 80 mV depolarizing current pulse. Pyramidal cells were distinguished based on the decay kinetics of the evoked current and by application of 10 μM CNQX at the end of the experiment.

Immunohistochemistry

Adult mice were anesthetized with pentobarbital and perfused with 4% PFA in 0.1 M phosphate buffer. The brain was removed and immersed in the same fixative for 4 h at 4°C and then cryoprotected in 20% sucrose in PBS

overnight at 4°C. 35-μm free-floating sections were cut on a sliding microtome. Endogenous peroxidase activity was inactivated by incubating brain sections in 0.5% H_2O_2 for 10 min. Sections were blocked for 1 h in PBS containing 3% normal goat serum and then incubated in the same buffer containing diluted 0.1 μg/ml MALS-3 antibody for 2 d at 4°C. Immunohistochemical staining was performed with an avidin/biotin/peroxidase system (ABC Elite; Vector Laboratories) and DAB (Vector Laboratories).

Online supplemental material

Fig. S1 shows the targeted disruption of the MALS-3 gene. Fig. S2 shows the colocalization of MALS and liprin-α with PSD-95. Online supplemental material is available at http://www.jcb.org/cgi/content/full/jcb.200503011/DC1.

The authors wish to thank David R.C. House for his technical help.

This work was supported by grants (to D.S. Bredt, R.A. Nicoll, O. Olsen, and K.A. Moore) from the National Institutes of Health and from the Christopher Reeves Paralysis Foundation (to D.S. Bredt).

The authors declare there is no financial conflict of interest related to this work.

Submitted: 3 March 2005
Accepted: 22 August 2005

References

Augustin, I., C. Rosenmund, T.C. Südhof, and N. Brose. 1999. Munc13-1 is essential for fusion competence of glutamatergic synaptic vesicles. *Nature.* 400:457–461.

Bekkers, J.M., and C.F. Stevens. 1991. Excitatory and inhibitory autaptic currents in isolated hippocampal neurons maintained in cell culture. *Proc. Natl. Acad. Sci. USA.* 88:7834–7838.

Borg, J.-P., Y. Yang, M. De Taddéo-Borg, B. Margolis, and R.S. Turner. 1998. The X11alpha protein slows cellular amyloid precursor protein processing and reduces Abeta40 and Abeta42 secretion. *J. Biol. Chem.* 273:14761–14766.

Borg, J.-P., M.O. Lõpez-Figueroa, M. de Taddèo-Borg, D.E. Kroon, R.S. Turner, S.J. Watson, and B. Ben Margolis. 1999. Molecular analysis of the X11-mLin-2/CASK complex in brain. *J. Neurosci.* 19:1307–1316.

Butz, S., M. Okamoto, and T.C. Südhof. 1998. A tripartite protein complex with the potential to couple synaptic vesicle exocytosis to cell adhesion in brain. *Cell.* 94:773–782.

Fannon, A.M., and D.R. Colman. 1996. A model for central synaptic junctional complex formation based on the differential adhesive specificities of the cadherins. *Neuron.* 17:423–434.

Flanagan, J.G., and P. Vanderhaeghen. 1998. The ephrins and Eph receptors in neural development. *Annu. Rev. Neurosci.* 21:309–345.

Garcia, R.A., K. Vasudevan, and A. Buonanno. 2000. The neuregulin receptor ErbB-4 interacts with PDZ-containing proteins at neuronal synapses. *Proc. Natl. Acad. Sci. USA.* 97:3596–3601.

Hata, Y., S. Butz, and T.C. Südhof. 1996. CASK: a novel dlg/PSD95 homolog with an N-terminal calmodulin-dependent protein kinase domain identified by interaction with neurexins. *J. Neurosci.* 16:2488–2494.

Ho, A., W. Morishita, R.E. Hammer, R.C. Malenka, and T.C. Südhof. 2003. A role for Mints in transmitter release: Mint 1 knockout mice exhibit impaired GABAergic synaptic transmission. *Proc. Natl. Acad. Sci. USA.* 100:1409–1414.

Ichtchenko, K., Y. Hata, T. Nguyen, B. Ullrich, M. Missler, C. Moomaw, and T.C. Südhof. 1995. Neuroligin 1: a splice site-specific ligand for beta-neurexins. *Cell.* 81:435–443.

Jo, K., R. Derin, M. Li, and D.S. Bredt. 1999. Characterization of MALS/Velis-1, -2, and -3: a family of mammalian LIN-7 homologs enriched at brain synapses in association with the postsynaptic density-95/NMDA receptor postsynaptic complex. *J. Neurosci.* 19:4189–4199.

Kaech, S.M., C.W. Whitfield, and S.K. Kim. 1998. The LIN-2/LIN-7/LIN-10 complex mediates basolateral membrane localization of the *C. elegans* EGF receptor LET-23 in vulval epithelial cells. *Cell.* 94:761–771.

Kaufmann, N., J. DeProto, R. Ranjan, H. Wan, and D. Van Vactor. 2002. *Drosophila* liprin-alpha and the receptor phosphatase Dlar control synapse morphogenesis. *Neuron.* 34:27–38.

Laverty, H.G., and J.B. Wilson. 1998. Murine CASK is disrupted in a sex-linked cleft palate mouse mutant. *Genomics.* 53:29–41.

Lee, S., S. Fan, O. Makarova, S. Straight, and B. Margolis. 2002. A novel and conserved protein-protein interaction domain of mammalian Lin-2/CASK binds and recruits SAP97 to the lateral surface of epithelia. *Mol. Cell. Biol.* 22:1778–1791.

Misawa, H., Y. Kawasaki, J. Mellor, N. Sweeney, K. Jo, R.A. Nicoll, and D.S. Bredt. 2001. Contrasting localizations of MALS/LIN-7 PDZ proteins in brain and molecular compensation in knockout mice. *J. Biol. Chem.* 276:9264–9272.

Missler, M., W. Zhang, A. Rohlmann, G. Kattenstroth, R.E. Hammer, K. Gottmann, and T.C. Südhof. 2003. Alpha-neurexins couple Ca^{2+} channels to synaptic vesicle exocytosis. *Nature.* 423:939–948.

Okamoto, M., and T.C. Südhof. 1997. Mints, Munc18-interacting proteins in synaptic vesicle exocytosis. *J. Biol. Chem.* 272:31459–31464.

Perego, C., C. Vanoni, S. Massari, R. Longhi, and G. Pietrini. 2000. Mammalian LIN-7 PDZ proteins associate with beta-catenin at the cell-cell junctions of epithelia and neurons. *EMBO J.* 19:3978–3989.

Rongo, C., C.W. Whitfield, A. Rodal, S.K. Kim, and J.M. Kaplan. 1998. LIN-10 is a shared component of the polarized protein localization pathways in neurons and epithelia. *Cell.* 94:751–759.

Schoch, S., P.E. Castillo, T. Jo, K. Mukherjee, M. Geppert, Y. Wang, F. Schmitz, R.C. Malenka, and T.C. Südhof. 2002. RIM1alpha forms a protein scaffold for regulating neurotransmitter release at the active zone. *Nature.* 415:321–326.

Serra-Pages, C., Q.G. Medley, M. Tang, A. Hart, and M. Streuli. 1998. Liprins, a family of LAR transmembrane protein-tyrosine phosphatase-interacting proteins. *J. Biol. Chem.* 273:15611–15620.

Setou, M., T. Nakagawa, D.-H. Seog, and N. Hirokawa. 2000. Kinesin superfamily motor protein KIF17 and mLin-10 in NMDA receptor-containing vesicle transport. *Science.* 288:1796–1802.

Shelly, M., Y. Mosesson, A. Citri, S. Lavi, Y. Zwang, N. Melamed-Book, B. Aroeti, and Y. Yarden. 2003. Polar expression of ErbB-2/HER2 in epithelia. Bimodal regulation by Lin-7. *Dev. Cell.* 5:475–486.

Südhof, T.C. 2004. The synaptic vesicle cycle. *Annu. Rev. Neurosci.* 27:509–547.

Tomita, S., L. Chen, Y. Kawasaki, R.S. Petralia, R.J. Wenthold, R.A. Nicoll, and D.S. Bredt. 2003. Functional studies and distribution define a family of transmembrane AMPA receptor regulatory proteins. *J. Cell Biol.* 161:805–816.

Torres, R., B.L. Firestein, J. Staudinger, H. Dong, E.N. Olson, R.L. Huganir, D.S. Bredt, N.W. Gale, and G.D. Yancopoulos. 1998. PDZ proteins bind, cluster and synaptically co-localize with Eph receptors and their ligands, the ephrins. *Neuron.* 21:1453–1463.

Tovar, K.R., and G.L. Westbrook. 1999. The incorporation of NMDA receptors with a distinct subunit composition at nascent hippocampal synapses in vitro. *J. Neurosci.* 19:4180–4188.

Wyszynski, M., E. Kim, A.W. Dunah, M. Passafaro, J.G. Valtschanoff, C. Serra-Pages, M. Streuli, R.J. Weinberg, and M. Sheng. 2002. Interaction between GRIP and liprin-alpha/SYD2 is required for AMPA receptor targeting. *Neuron.* 34:39–52.

Zhen, M., and Y. Jin. 1999. The liprin protein SYD-2 regulates the differentiation of presynaptic termini in *C. elegans*. *Nature.* 401:371–375.

ELSEVIER

Neurobiology of Disease

www.elsevier.com/locate/ynbdi
Neurobiology of Disease 23 (2006) 169 177

Conditional knockout of Mn superoxide dismutase in postnatal motor neurons reveals resistance to mitochondrial generated superoxide radicals

Hidemi Misawa,[a,b,*] Kazuko Nakata,[a] Junko Matsuura,[a] Yasuhiro Moriwaki,[b] Koichiro Kawashima,[b] Takahiko Shimizu,[c] Takuji Shirasawa,[c] Ryosuke Takahashi[d,e]

[a]*Department of Neurology, Tokyo Metropolitan Institute for Neuroscience, 2-6, Musashidai, Fuchu-shi, Tokyo 183-8526, Japan*
[b]*Department of Pharmacology, Kyoritsu University of Pharmacy, 1-5-30, Shibakoen, Minato-ku, Tokyo 105-8512, Japan*
[c]*Department of Molecular Gerontology, Tokyo Metropolitan Institute of Gerontology, 35-2, Sakae-cho, Itabashi-ku, Tokyo 173-0015, Japan*
[d]*Laboratory for Motor System Neurodegeneration, RIKEN Brain Science Institute, 2-1, Hirosawa, Wako-shi, Saitama 351-0198, Japan*
[e]*Deparment of Neurology, Graduate School of Medicine, Kyoto University, 54, Sho-goin kawaramachi, Sakyo-ku, Kyoto 606-8507, Japan*

Received 22 November 2005; revised 24 January 2006; accepted 27 February 2006
Available online 3 May 2006

Mitochondrial dysfunction and oxidative damage are implicated in the pathogenesis of neurodegenerative disease. Mice deficient in the mitochondrial form of superoxide dismutase (SOD2) die during embryonic or early postnatal development, precluding analysis of a pathological role for superoxide in adult tissue. Here, we generated postnatal motor neuron-specific SOD2 knockouts by crossing mice with floxed SOD2 alleles to VAChT-Cre transgenic mice in which Cre expression is restricted to postnatal somatomotor neurons. SOD2 immunoreactivity was specifically lost in a subset of somatomotor neurons resulting in enhanced superoxide production. Yet extensive histological examination revealed no signs of oxidative damage in animals up to 1 year after birth. However, disorganization of distal nerve axons following injury was accelerated in SOD2-deficient motor neurons. These data demonstrate that postnatal motor neurons are surprisingly resistant to oxidative damage from mitochondrial-derived superoxide radicals, but that such damage may sensitize axons to disorganization following nerve injury.

Keywords: Motor neurons; Oxidative stress; Mitochondria; Nerve injury; Conditional knockout; SOD2; Amyotrophic lateral sclerosis

Introduction

Oxygen radicals, of which superoxide ($O_2^{\bullet -}$) is the most abundant, are a natural byproduct of oxygen consumption by the respiratory chain in aerobic ATP production. The superoxide dismutases (SODs) are enzymes that catalyze the conversion of $O_2^{\bullet -}$ to hydrogen peroxide and thus help prevent the build up of toxic $O_2^{\bullet -}$ levels. Three SOD isoforms are expressed in mammalian cells: copper/zinc SOD (SOD1) located in the cytoplasm (McCord and Fridovich, 1969), manganese SOD (SOD2) located in the mitochondrial matrix (Weisiger and Fridovich, 1973) and extracellular SOD (SOD3) (Marklund, 1982; Hjalmarsson et al., 1987). A small fraction of SOD1 is also reported to reside in the intermembrane space of mitochondria (Okado-Matsumoto and Fridovich, 2001; Mattiazzi et al., 2002; Okado-Matsumoto and Fridovich, 2002).

Oxidative stress has been implicated in various neurodegenerative diseases including Parkinson's disease, Alzheimer's disease and amyotrophic lateral sclerosis (ALS). Though it remains unclear whether oxidative stress is a major cause or merely a consequence of cellular dysfunction associated with neurodegenerative diseases (Andersen, 2004), an accumulating body of evidence implicates impaired mitochondrial energy production and increased mitochondrial oxidative damage in early pathological events leading to neurodegeneration (Beal, 1996). Mitochondria are both a major source of reactive oxygen species (ROS) production as well as a major target of ROS-induced cellular injury. Thus, mitochondrial localized superoxide dismutase (SOD2) is thought to play an important role in cellular defense against oxidative damage by ROS.

Loss of SOD2 results in embryonic or early postnatal lethality that varies with genetic background. SOD2 knockout mice on a CD-1 background die either in utero or within 24 h after birth from severe dilated cardiomyopathy (Li et al., 1995). Similarly, C57BL/6 SOD2 knockout mice die at late embryonic or early neonatal stages from dilated cardiomyopathy (Huang et al., 2001; Ikegami et al., 2002). On a mixed C57BL/6 and 129/Sv background, SOD2 mutant mice survive for up to 18 days, develop a milder form of

* Corresponding author. Department of Pharmacology, Kyoritsu University of Pharmacy, 1-5-30, Shibakoen, Minato-ku, Tokyo 105-8512, Japan. Fax: +81 3 5400 2698.
E-mail address: misawa-hd@kyoritsu-ph.ac.jp (H. Misawa).
Available online on ScienceDirect (www.sciencedirect.com).

0969-9961/$ - see front matter © 2006 Elsevier Inc. All rights reserved.
doi:10.1016/j.nbd.2006.02.014

dilated cardiomyopathy and display a neurological phenotype (Lebovitz et al., 1996). In contrast, DBA/2J (D2) SOD2 mutant mice do not develop cardiomyopathy but instead develop severe metabolic acidosis and survive an average of 8 days (Huang et al., 2001). This phenotypic variation suggests that sensitivities to SOD2 deficiency are highly dependent on genetic modifiers that differ across strain and cell type.

Motor neurons are believed to be particularly susceptible to oxidative damage given the high metabolic requirement to sustain a large cell size and long axonal processes. Although motor neurons in cell culture are vulnerable to cell death mediated via calcium influx after exposure to glutamate, it is unclear how motor neurons respond to the overproduction of mitochondrial-derived ROS in vivo. To circumvent the early lethality of SOD2 knockout mice, we used a conditional gene deletion approach in which mice with floxed SOD2 genes (Ikegami et al., 2002) were mated with VAChT-Cre mice (Misawa et al., 2003) that express Cre recombinase in approximately 50% of postnatal somatic motor neurons. Here, we report that conditional loss of SOD2 in postnatal motor neurons results in elevated mitochondrial oxidative stress that fails to trigger signs of neurodegeneration under nonpathological conditions. In contrast, nerve axotomy revealed accelerated nerve disorganization, suggesting that adult motor neurons have relative resistance to mitochondrial-generated superoxide radicals unless stressed.

Materials and methods

Mice

C57BL/6 mice carrying the VAChT-Cre transgene (VAChT-Cre.Fast and VAChT-Cre.Slow) have been described previously (Misawa et al., 2003). C57BL/6 mice with floxed SOD2 alleles have been described elsewhere (Ikegami et al., 2002). Localization of the VAChT-Cre transgene in the VAChT-Cre.Slow mouse line to chromosome 4 was determined by FISH analysis (data not shown), and VAChT-Cre.Slow mice were used to direct motor neuron-specific Cre expression in this study. Homozygous floxed SOD2 mice (lox/lox) were crossed with VAChT-Cre.Slow heterozygote animals. The resulting double heterozygote animals ($SOD2^{lox/+}$; $Cre^{slow/-}$) were selected and mated with homozygote floxed SOD2 mice. All animals were genotyped for SOD2 allele (Ikegami et al., 2002) and the Cre transgene (Misawa et al., 2003) using tail DNA as described previously. Motor performance was analyzed using a rotarod treadmill (MK-600; Muromachi Kikai, Tokyo, Japan) at 28 rpm. Grip strength was measured using a Grip Strength Meter for Mouse (Model 57106; Stoelting, Wood Dale, IL). All animal protocols were approved by the Tokyo Metropolitan Institute for Neuroscience Institutional Animal Care and Use Committee.

Histological assessment and immunohistochemistry

Mice were anesthetized with sodium pentobarbital and perfused through the aortic cone with phosphate-buffered saline (PBS), followed with 4% paraformaldehyde (PFA) in 0.1 M phosphate buffer (PB) at pH 7.4. Brains and spinal cords were removed and postfixed in the same fixative for 2 h and then immersed in 20% sucrose in PB overnight at 4°C. The tissue was sectioned at 20 μm on a freezing microtome. For paraffin-embedded section, tissues were transferred to 70% ethanol and embedded in paraffin as described (Ichikawa et al., 1997). Serial brain or spinal cord sections were cut at 5 μm. Sections were stained for Nissl substance with cresyl violet or Fluoro-Jade B (Chemicon) according to the manufacturer's protocol. For staining of SOD2, SOD1, ChAT, and CHT, paraffin-embedded sections were immunohistochemically processed as described elsewhere (Ichikawa et al., 1997) with diaminobenzidine (DAB) as a chromogen followed by poststaining with hematoxylin. Antibodies used are rabbit polyclonal anti-SOD2 antibody (1:2000; Stressgen Biotechnologies), rabbit polyclonal anti-SOD1 antibody (1:2000; Stressgen Biotechnologies), rabbit polyclonal anti-ChAT (1:10,000; Ichikawa et al., 1997), and rabbit polyclonal anti-CHT antibody (50 ng/ml; Misawa et al., 2001). To estimate frequencies of Cre-mediated recombination of the floxed SOD2 alleles, serial paraffin sections were stained with SOD2 and ChAT as above, and the number of positive cells was counted. More than 500 cells were analyzed in the spinal cord ventral horn and 200 cells in each of the brainstem motor nucleus (from at least 3 mice at respective age). Double labeling for SOD2 and SMI-32 was performed by immunofluorescence. Sections were incubated simultaneously with rabbit polyclonal anti-SOD2 antibody (1:500; Stressgen Biotechnologies) and mouse SMI-32 monoclonal antibody to neurofilaments (1:1,000; Sternberger Monoclonals). Texas red-conjugated goat anti-mouse IgG was used to detect SMI-32-positive cells, and fluorescein isothiocyanate-conjugated goat anti-rabbit IgG was used to detect SOD2-expressing cells (1:200; Jackson Immunoresearch Labs).

In situ detection of $O_2^{\bullet-}$ production

The spatial production of $O_2^{\bullet-}$ was investigated by in situ detection of oxidized hydroethidine (HEt; Molecular Probes) as previously described (Murakami et al., 1998). HEt is oxidized to a red fluorescent dye (ethidium) in living cells selectively by $O_2^{\bullet-}$, but not by other reactive oxygen species such as hydrogen peroxide, hydroxyl radical, or peroxynitrite (Bindokas et al., 1996). Briefly, HEt solution (0.2 ml; stock solution of HEt, 100 mg/ml in DMSO, diluted to 1 mg/ml in PBS) was intravenously injected 30 min before the animals were sacrificed. The animals were perfused with 4% paraformaldehyde as described above. Brain and spinal cord sections (20 μm) were cut on a cryostat and processed for fluorescent microscopy.

Hypoglossal nerve axotomy

Nine-month-old mice ($SOD2^{lox/lox}$;$Cre^{slow/-}$ or $SOD2^{lox/lox}$; $Cre^{-/-}$) were anesthetized with an intraperitoneal injection of ketamine (80 mg/kg) and xylazine (12 mg/kg). The right hypoglossal nerve was exposed under the digastric muscle and transected with scissors. After 5 weeks, the animals were reanesthetized and perfused with 4% paraformaldehyde. The brainstem was removed, 5-μm serial paraffin-embedded sections were prepared and stained with cresyl violet as described above. Hypoglossal motor neurons with distinct clear nuclei in every eighth section (total 8 sections per animal) were counted.

Analysis of Wallerian degeneration

Two days after unilateral transection of hypoglossal nerves as described above, mice were sacrificed by over-dose of sodium pentobarbital, the swollen first 2 mm of the distal nerve was discarded, the next 2 mm was used for morphological analysis, and a segment 4–7 mm distal to the lesion site was used for Western blotting. For morphological analysis, the nerve segments were fixed

for 1 day in 2% paraformaldehyde, 2% glutaraldehyde in 50 mM phosphate buffer, pH 7.4 (PB). Samples were treated in 1% OsO_4 in PB, washed, dehydrated with ethanol and then propylene oxide, and finally embedded in Quetol 812 epoxy resin (Nisshin EM, Tokyo, Japan). Semithin cross-sections (0.5 μm) for light microscopy were stained with toluidine blue.

Electron microscopy

Animals were perfused with 2% glutaraldehyde, 2% paraformaldehyde, 5% sucrose in 50 mM phosphate buffer (pH 7.4). The brain and spinal cord were removed and postfixed in the same fixative for 1 d at 4°C. The facial nucleus and spinal cord ventral horn were cut into 1- to 2-mm square pieces, fixed in 1% osmium tetroxide for 1 h at 4°C, dehydrated through a graded series of ethanol solutions and into propylene oxide, and embedded in Quetol 812 (Nissin EM). Ultra-thin sections were stained with lead citrate and uranyl acetate and examined with an electron microscope (H7500; Hitachi, Tokyo, Japan) at 10,000× magnification.

Analysis of muscle atrophy and denervation

Fresh skeletal muscle biopsies were obtained and frozen by immersion in isopentane cooled in liquid nitrogen. Sections were

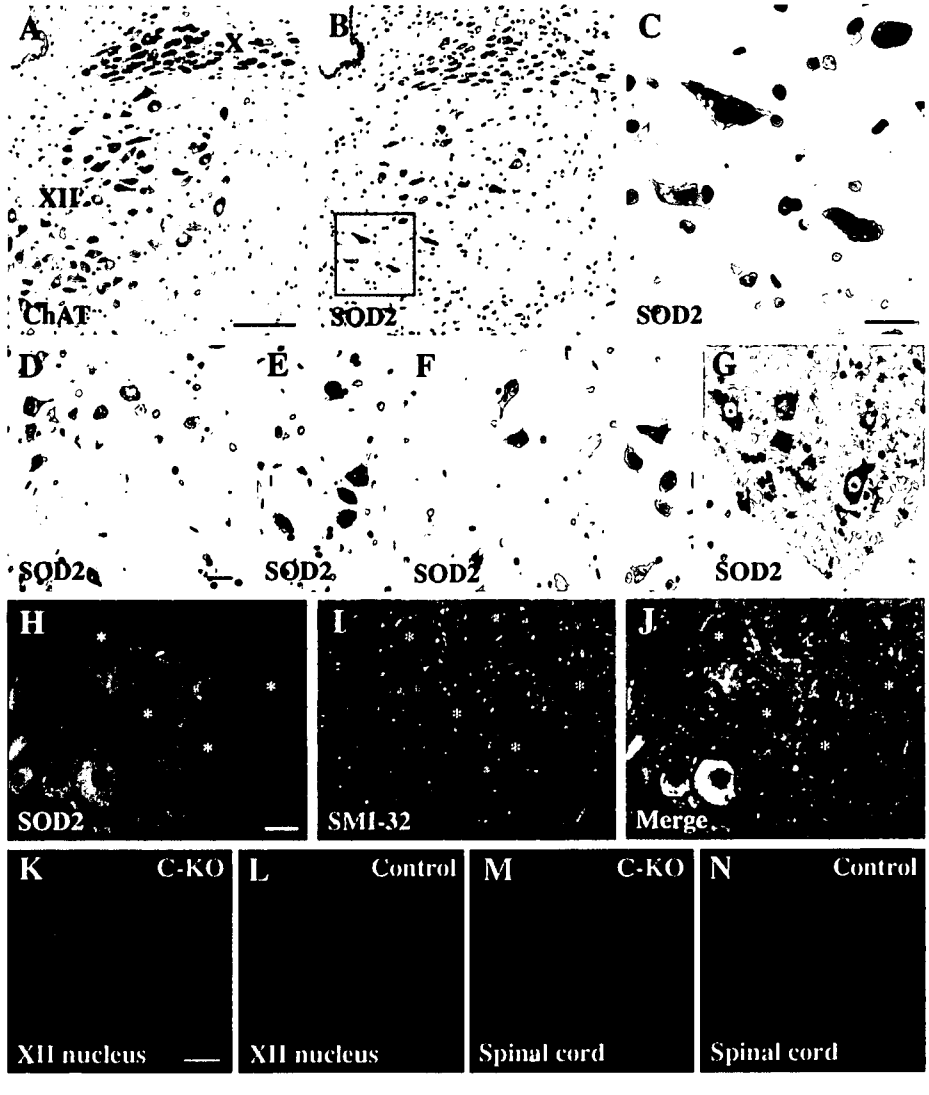

Fig. 1. Loss of SOD2 immunoreactivity in motor neurons from $SOD2^{lox/lox}$;$Cre^{slow/-}$ mice. (A–G) Paraffin-embedded sections of brain and spinal cord from $SOD2^{lox/lox}$;$Cre^{slow/-}$ mice at 5 months old stained with anti-ChAT antibody (A) or anti-SOD2 antibody (B-G). SOD2 immunoreactivity was lost in a subset of ChAT-positive somatomotor neurons as revealed by serial section through the hypoglossal nuclei (A–C) as well as sections through the oculomotor (D), abducens (E), facial (F) nuclei, and the ventral horn of the spinal cord (G). Note that SOD2 immunoreactivity was preserved in visceromotor neurons in the dorsal motor nucleus of the vagus (B). X, dorsal motor nucleus of the vagus; XII, hypoglossal nucleus. The boxed area in B is enlarged in panel C. (H–J) Paraffin-embedded sections from the ventral horn of the spinal cord were double-stained by immunofluorescence with anti-SOD2 (H) and anti-SMI-32 (I) antibodies. The merged image is shown in panel J. SOD2 immunoreactivity was lost in a subset of SMI-32-positive large motor neurons (denoted by asterisks) but not in SMI-32-negative small-diameter interneurons. (K–N) Mitochondrial production of $O_2^{\bullet}$ was increased in $SOD2^{lox/lox}$;$Cre^{slow/-}$ (C-KO) mice compared with $SOD2^{lox/lox}$;$Cre^{-/-}$ (Control) mice in motor neurons in the hypoglossal nucleus (K and L) and ventral horn of the spinal cord (M and N) as revealed by HEt oxidation. HEt signals were detected in motor neurons as small granular particles in the cytosol, indicating mitochondrial production of $O_2^{\bullet-}$ under normal physiological conditions. Scale bars = 100 μm (A; also applies to B); 20 μm (C); 20 μm (D; also applies to E–G); 20 μm (H; also applies to I, J); 20 μm (K; also applies to L–N).

cut at 10 μm and processed for hematoxylin–eosin (H&E) or Gomori trichrome staining.

Western blotting

Cytoskeletal protein preservation was determined as described by Mack et al. (2001). Briefly, axotomized or control (uncut) hypoglossal nerves (3-mm length) were homogenized in 50 μl 25 mM Tris–HCl (pH 7.5), 2% SDS, 1 mM EDTA, 1× Complete protease inhibitor cocktail (Roche). Proteins (20 μl each) were separated using a 5–20% gradient polyacrylamide-SDS gel and semi-dry transferred onto a nylon membrane (Immobilon-P; Millipore). Loading and transfer were checked by staining with Ponceau S (Sigma). The membranes were incubated with monoclonal N52 antibody (Sigma) against neurofilament heavy chain diluted at 1:3000 in 5% nonfat skim milk/0.1% Tween 20 in PBS, followed by incubation with horseradish peroxidase-conjugated anti-mouse IgG (Bio-Rad), and visualized with ECL Western Blotting Detection Reagent (Amersham Pharmacia Biosciences). The same blots were reprobed with monoclonal antibody β-tub 2.1 (1:10,000; Sigma) against β-tubulin. In order to compare SOD2 expression between $SOD2^{lox/lox}$;$Cre^{slow/-}$ and $SOD2^{lox/lox}$;$Cre^{-/-}$ mice, ventral halves of the cervical spinal cord (5-mm length) were micro-dissected, homogenized, and processed for immunoblot analysis as described above with rabbit polyclonal anti-SOD2 antibody (1:10,000; Stressgen Biotechnologies), rabbit polyclonal anti-SOD1 antibody (1:10,000; Stressgen Biotechnologies), and mouse monoclonal anti-actin antibody (1 μg/ml; Chemicon).

Results

Generation of motor neuron-specific SOD2 knockout mice

To generate postnatal motor neuron-specific SOD2 knockout mice, we crossed mice homozygous for floxed SOD2 alleles (Ikegami et al., 2002) with VAChT-Cre.Slow mice in which Cre expression is restricted in postnatal somatomotor neurons (Misawa et al., 2003). The VAChT-Cre.Fast line was not used in this study because the transgene integrated on the same chromosome as SOD2 (chromosome 17). Double heterozygote animals ($SOD2^{lox/+}$;$Cre^{slow/-}$) were again mated with homozygous floxed SOD2 mice. $SOD2^{lox/lox}$;$Cre^{slow/-}$ mice were born at a Mendelian ratio and survived to adulthood with no gross defects (data not shown). Furthermore, no signs of motor deficits, including tremor and paralysis, or muscle weakness were observed for up to 12 months as revealed by a rotarod test and grip strength measurements, respectively. Motor neurons in $SOD2^{lox/lox}$;$Cre^{slow/-}$ mice showed normal cell morphology, including soma size, and normal immunoreactivity for cholinergic markers such as choline acetyltransferase (ChAT; Figs. 1A and 2A–F), vesicular acetylcholine transporter (VAChT) and high-affinity choline transporter (CHT). In the brain stem and spinal cord, approximately 50% of ChAT-positive motor neurons lost mitochondrial SOD2 immunoreactivity, suggesting successful targeting of the SOD2 gene (Figs. 1A–J). The SOD2-negative motor neurons were observed in various somatomotor nuclei of the brainstem and spinal cord, but not in visceromotor nuclei such as the dorsal motor nucleus of the vagus. Also double immunofluorescence for SOD2 and SMI-32 (a marker for motor

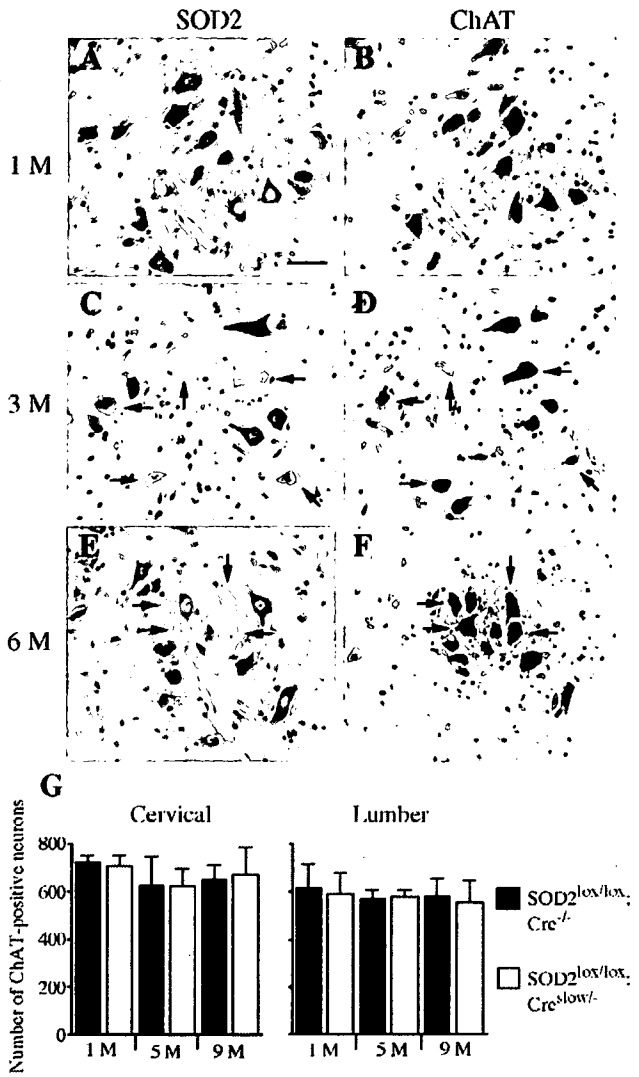

Fig. 2. Detection of SOD2-deficient and ChAT-positive motor neurons in the spinal cord of $SOD2^{lox/lox}$;$Cre^{slow/-}$ mice. Serial paraffin-embedded 5-μm sections of the lumber spinal cord from $SOD2^{lox/lox}$;$Cre^{slow/-}$ mice at 1 month (A, B), 3 months (C, D), or 6 months (E, F) of age were stained with anti-SOD2 (A, C, E) or anti-ChAT (B, D, F) antibodies. Arrows indicate SOD2-negative and ChAT-positive motor neurons. Scale bar = 50 μm. (G) Numbers of spinal cord ChAT-positive motor neurons in $SOD2^{lox/lox}$;$Cre^{slow/-}$ and $SOD2^{lox/lox}$;$Cre^{-/-}$ mice. Numbers were determined from every 5th section for a total of 15 sections. Shown are the means from three mice ± standard deviation (n = 3).

neurons) reveals that SOD2 immunoreactivity was lost specifically in SMI-32-positive motor neurons and not in SMI-32-negative spinal interneurons (Figs. 1H–J).

Increased production of $O_2^{\bullet -}$ by mitochondria in $SOD2^{lox/lox}$; $Cre^{slow/-}$ mice

To examine the effect of loss of SOD2 on superoxide production, we compared the spatial production of $O_2^{\bullet -}$ between $SOD2^{lox/lox}$; $Cre^{slow/-}$ and $SOD2^{lox/lox}$; $Cre^{-/-}$ mice by using HEt, a $O_2^{\bullet -}$-specific fluorescent dye (Figs. 1K–N). In the brainstem and spinal cord, punctate ethidium signals in the cytosol reflecting mitochondrial production of $O_2^{\bullet -}$ were detected in motor neurons with large somas, suggesting a relatively high mitochondrial respiratory rate in these

cells under normal physiological conditions. The cytosolic punctate fluorescence of oxidized HEt was more intense in SOD2$^{lox/lox}$;Cre$^{slow/-}$ mice compared to SOD2$^{lox/lox}$;Cre$^{-/-}$ mice in a subset of hypoglossal and spinal cord motor neurons, confirming enhanced production of $O_2^{\bullet-}$ by mitochondria in SOD2$^{lox/lox}$;Cre$^{slow/-}$ mice. On the other hand, this increase in HEt fluorescence was not observed in visceral motor neurons such as the dorsal motor nucleus of the vagus in SOD2$^{lox/lox}$;Cre$^{slow/-}$ mice (data not shown).

Normal neurological and neurochemical profile of SOD2$^{lox/lox}$;Cre$^{slow/-}$ mice

Despite the loss of SOD2 expression and increased superoxide production in motor neurons by 3 months of age (Figs. 2A–F), the number of ChAT-positive motor neurons in the cranial and lumber spinal cord was not significantly different between SOD2$^{lox/lox}$;Cre$^{slow/-}$ and SOD2$^{lox/lox}$;Cre$^{-/-}$ mice at either 5 or 9 months of age (Fig. 2G). Neither overt cell loss nor vacuolar changes in neurons or neuropil were observed as revealed by Nissl-staining of SOD2-negative motor neurons (Figs. 3A–D). Also analyzed was neuronal degeneration by Fluoro-Jade B (Schmued et al., 1997). No Fluoro-Jade B-positive neurons were detected in brain and spinal cord sections from either SOD2$^{lox/lox}$;Cre$^{slow/-}$ or SOD2$^{lox/lox}$; Cre$^{-/-}$ mice (not shown).

As free radicals are a potential source of damage to cellular constituents such as DNA, lipids, and proteins, we evaluated SOD2$^{lox/lox}$;Cre$^{slow/-}$ mice for histochemical signs of oxidative injury and stress. Yet SOD2-deficient motor neurons failed to react with any of the following antibodies: anti-SMI-31 monoclonal antibodies (Sternberger Monoclonals) to phosphorylated neurofilaments which are shown to be accumulated in nerve cell bodies under pathological conditions; a monoclonal antibody against 8-hydroxy-2-deoxyguanosine (8-OHdG; JAICA, Shizuoka, Japan) to oxidative DNA damage; a polyclonal anti-malondialdehyde antibody (MDA; Alpha Diagnostic International, San Antonio, TX) to lipid peroxidation-related MDA-protein adduct; or a monoclonal anti-nitrotyrosine antibody (Upstate Cell Signaling, Lake Placid, NY) to peroxynitrite-mediated protein modification.

A small fraction of SOD1 is reported to reside in the intermembranous space of mitochondria (Okado-Matsumoto and Fridovich, 2001; Mattiazzi et al., 2002; Okado-Matsumoto and Fridovich, 2002) where it may work as an additional line of defense against $O_2^{\bullet-}$. However, immunohistochemical staining showed no obvious compensatory overexpression of SOD1 in the SOD2-deficient motor neurons (Figs. 3E and F). It is still tempting to speculate that an increased amount of SOD1 is accumulated in mitochondria under the SOD2-deficient conditions. A detailed analysis of SOD2 subcellular localization using confocal microscopy or immunoelectron microscopy will be needed to address the possibility.

Next, we analyzed SOD2 expression in ventral halves of the cervical spinal cord micro-dissected from 9-month-old SOD2$^{lox/lox}$; Cre$^{slow/-}$ and SOD2$^{lox/lox}$;Cre$^{-/-}$ mice by immunoblot analysis (Fig. 3G). A significant decrease (30% by densitometry) in SOD2 content was evident in SOD2$^{lox/lox}$;Cre$^{slow/-}$ mice, although again SOD1 expression was unchanged. Even though SOD2 immunoreactivity is most strong in motor neurons in spinal cord sections, the homogenates include mitochondria from various other cell types such as glia and interneurons. Thus, the result shows that SOD2 expression was lost in 30% of the spinal motor neurons at the very least.

Finally, an ultrastructural analysis of mitochondria in motor neurons was undertaken using electron microscopy. Sections of the facial nucleus and spinal cord from 9-month-old SOD2$^{lox/lox}$; Cre$^{slow/-}$ and SOD2$^{lox/lox}$;Cre$^{-/-}$ mice were analyzed. Over 1000 mitochondria in each brain regions were examined, but no degenerative changes such as swelling, disorganization of the cristae or vacuolar formation were observed (n = 3 for each genotype; data not shown).

As no obvious phenotype was detected in the cell bodies or organelles of SOD2-deficient motor neurons, we next analyzed the function of axonal processes by looking for muscle denervation and atrophy. Muscle biopsies from SOD2$^{lox/lox}$;Cre$^{slow/-}$ mice revealed

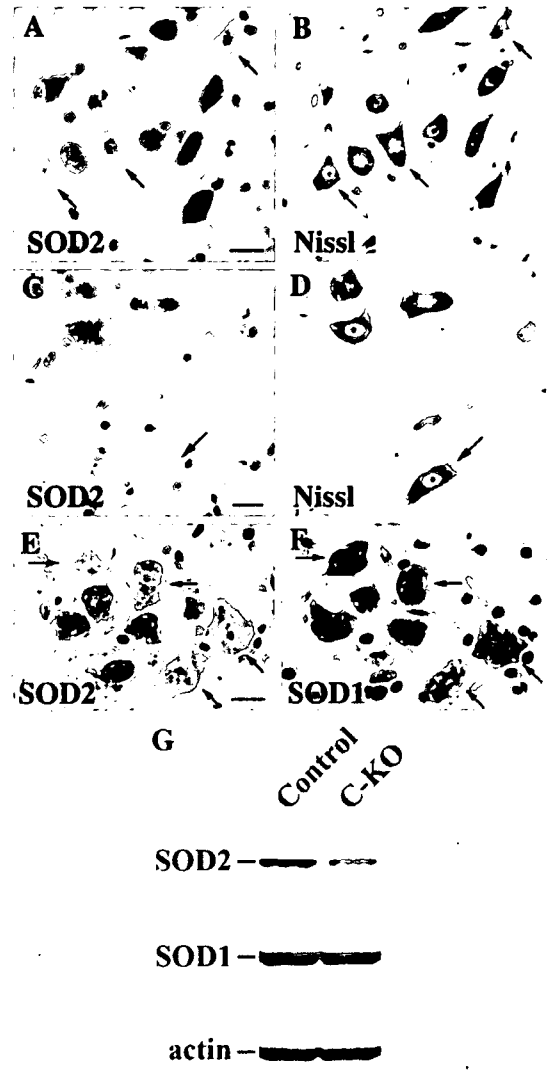

Fig. 3. Morphology of SOD2-deficient motor neurons in 9-month-old SOD2$^{lox/lox}$;Cre$^{slow/-}$ mice. Serial sections from the facial nucleus (A, B) or spinal cord ventral horn (C, D) stained with an anti-SOD2 antibody (A, C) or cresyl violet (Nissl; B, D). No overt morphological changes were seen in the SOD2-defiecent motor neurons (arrows). Serial sections from the hypoglossal nucleus stained with anti-SOD2 (E) or anti-SOD1 (F) antibodies. No difference in the staining pattern or intensity was evident between SOD2-negative (arrows) and SOD2-positive motor neurons. Scale bars 20 μm. (G) Ventral portions of the spinal cord were micro-dissected from SOD2$^{lox/lox}$;Cre$^{slow/-}$ (C-KO) and SOD2$^{lox/lox}$;Cre$^{-/-}$ (Control) mice. Total homogenates (10 μg) were subjected to immunoblot analysis with polyclonal anti-SOD2 or anti-SOD1 antibodies. Actin content is shown as a loading control.

neither signs of muscle degeneration nor denervation/remodeling of motor axon terminals (Fig. 4). Furthermore, no evidence of reactive gliosis was revealed in $SOD2^{lox/lox}$;$Cre^{slow/-}$ mice by GFAP staining (data not shown), despite its presence in the brainstem motor nuclei of SOD2-null mice (Melov et al., 1998; Lynn et al., 2005).

Motor neuron survival after hypoglossal nerve axotomy is unchanged

Motor neurons in SOD1-deficient mice show an increased vulnerability to facial nerve axotomy despite an otherwise normal phenotype (Reaume et al., 1996). To test whether SOD2-deficient motor neurons are also more vulnerable to nerve injury, we employed unilateral transection of the hypoglossal nerve. Hypoglossal motor neuron survival was then assessed 5 weeks following transection (Fig. 5). Cell number in the axotomized hypoglossal nucleus decreased by approximately 10% compared to the contralateral control side, yet no statistical difference between $SOD2^{lox/lox}$;$Cre^{slow/-}$ and $SOD2^{lox/lox}$;$Cre^{-/-}$ mice was observed (Fig. 5). Furthermore, no difference in the number of SOD2-immunonegative cells was detected in $SOD2^{lox/lox}$;$Cre^{slow/-}$ mice after unilateral axotomy, and similar numbers of atrophic cells were seen in the transected nuclei of $SOD2^{lox/lox}$;$Cre^{slow/-}$ and $SOD2^{lox/lox}$;$Cre^{-/-}$ mice (data not shown).

Motor nerve axon disorganization is accelerated after hypoglossal nerve axotomy

Next, we analyzed the structural stability of the transected hypoglossal axon 2–4 mm distal to the lesion site 2 days postoperation. The distal segment of an injured nerve is known

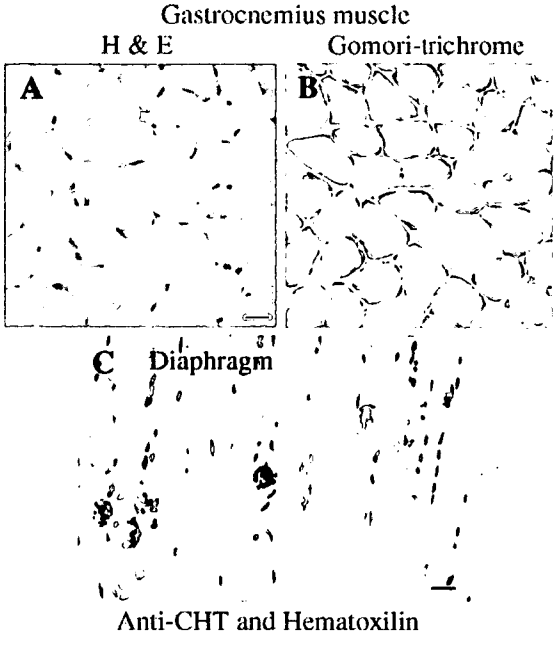

Fig. 4. Absence of muscle atrophy and denervation/remodeling of endplates in $SOD2^{lox/lox}$;$Cre^{slow/-}$ mice. Serial cryosections of gastrocnemius muscle from a 9-month-old $SOD2^{lox/lox}$;$Cre^{slow/-}$ mouse stained with hematoxylin and eosin (A) or Gomori-trichrome (B). Paraffin-embedded sections (5 μm) of diaphragm muscle containing neuromuscular junction from 9-month old $SOD2^{lox/lox}$;$Cre^{slow/-}$ mice stained with an anti-CHT antibody followed by counter-staining with hematoxylin (C). Scale bar = 20 μm.

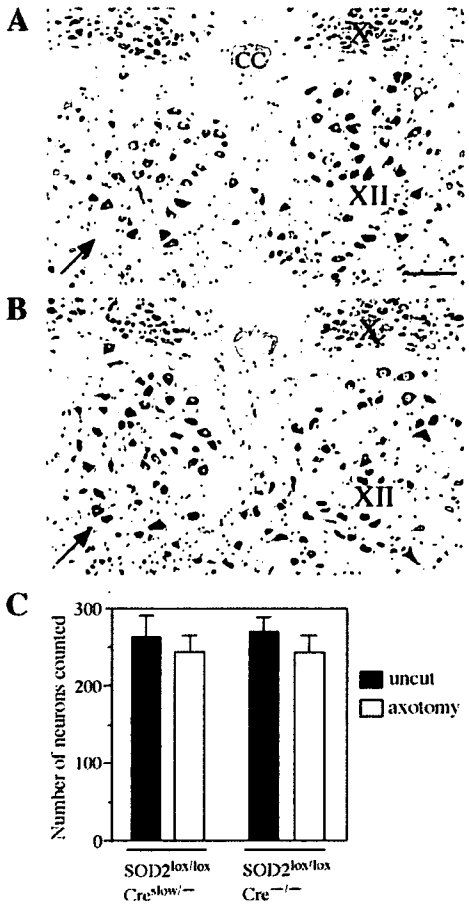

Fig. 5. Nissl-staining of hypoglossal motor neurons 5 weeks after axotomy in $SOD2^{lox/lox}$;$Cre^{slow/-}$ (A) and $SOD2^{lox/lox}$;$Cre^{-/-}$ (B) mice. Arrows indicate the operated side. CC, central canal; X, dorsal motor nucleus of the vagus; XII, hypoglossal nucleus. Scale bar = 100 μm. (C) Number of neurons in hypoglossal nuclei (uncut control or axotomized operated side) from both $SOD2^{lox/lox}$;$Cre^{slow/-}$ and $SOD2^{lox/lox}$;$Cre^{-/-}$ mice (n = 4 for each genotype).

to undergo Wallerian degeneration within a few days. In the uncut contralateral nerve, we observed no difference in axon number and diameter between $SOD2^{lox/lox}$;$Cre^{slow/-}$ and $SOD2^{lox/lox}$;$Cre^{-/-}$ mice. However, $SOD2^{lox/lox}$;$Cre^{slow/-}$ axons did show an accelerated degeneration after nerve injury. When compared with $SOD2^{lox/lox}$;$Cre^{-/-}$ mice both cytoskeletal protein stability as revealed by Western blot and axon structure as revealed by histological analysis were significantly altered (Fig. 6).

Discussion

The present study demonstrates for the first time that SOD2 is not required for postnatal motor neurons survival and further reveals that motor neurons are, in fact, quite resistant to mitochondrial generated $O_2^{\bullet-}$ in vivo. In the absence of SOD enzymatic activity, $O_2^{\bullet-}$ is relatively stable. Other antioxidants such as glutathione, ascorbate and tocopherols are relatively inefficient in removing superoxide radicals, and spontaneous dismutation occurs only very slowly. Because a portion of enzymatically active SOD1 is detected in the mitochondrial intermembranous space (Okado-Matsumoto and Fridovich, 2001; Mattiazzi

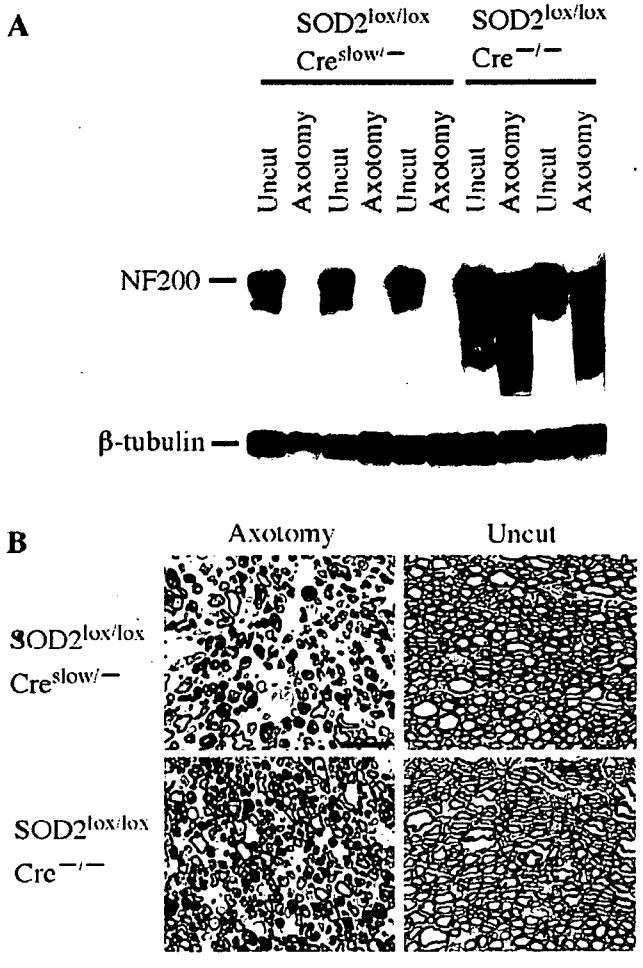

Fig. 6. Accelerated axonal disorganization in $SOD2^{lox/lox}$;$Cre^{slow/-}$ mice after motor nerve injury. (A) Western blot of 200-kDa neurofilament protein (NF-200) demonstrating the extent of degeneration 2 days after nerve transection in the distal transected hypoglossal nerve (Axotomy) or corresponding contralateral uncut nerve (Uncut). The blot was reprobed with control monoclonal antibody (β-tub 2.1) against β-tubulin. Samples from three $SOD2^{lox/lox}$;$Cre^{slow/-}$ and two $SOD2^{lox/lox}$;$Cre^{-/-}$ control mice are shown. (B) Representative toluidine blue-stained sections of hypoglossal nerves 2–4 mm distal to the lesion site 2 days after transection or corresponding contralateral uninjured nerve. Scale bar = 20 μm.

et al., 2002; Okado-Matsumoto and Fridovich, 2002), we speculate that, although the physiological functions of SOD1 in the mitochondria are not fully understood, some SOD2 function is compensated by SOD1 potentially by removing $O_2^{\bullet-}$ generated from complex III (Han et al., 2001). And although we did not detect SOD1 upregulation in SOD2-deficient motor neurons (Figs. 3E and F), endogenous levels of mitochondrial SOD1 may be sufficient to prevent both $O_2^{\bullet-}$-induced mitochondrial injury and $O_2^{\bullet-}$ release from mitochondria to cytosol. The physiological role and possible compensation of SOD2 loss by SOD1 can be addressed in future studies by crossing $SOD2^{lox/lox}$;$Cre^{slow/}$ mice to a SOD1-null background.

Motor neurons in the SOD1-deficient mice are vulnerable to axotomy-induced oxidative burden (Reaume et al., 1996). In the present study, we have analyzed the effect of nerve transection on motor neurons lacking SOD2 expression. We demonstrate here that neuronal survival after axotomy is not affected, but that disorganization of distal nerve axons is accelerated in the SOD2-deficient motor neurons. Thus, loss of SOD2 function is insufficient to kill transected motor neurons but does trigger more rapid motor axon degeneration after nerve injury. Although we do not yet understand the mechanism underlying the observed accelerated disorganization, we speculate that abnormal Ca^{2+} handling in SOD2-deficient mitochondria results in lowered Ca^{2+}-buffering activity specifically in lesioned distal axons while leaving the cell bodies unaffected. Interestingly, neurofilament proteins are known to be particularly susceptible tyrosine nitration and lysine oxidation (Beckman et al., 1993). Our present study thus implicates a previously unrecognized link between mitochondrial oxidative stress and axonal vulnerability to injury.

ALS is a fatal adult-onset neurodegenerative disease characterized by the selective loss of upper and lower motor neurons. Although its cause is not fully understood, mutations in the SOD1 gene cause a familial form of ALS, and recent studies show involvement of mitochondrial dysfunction and oxidative damage in ALS pathogenesis (Andersen, 2004; Bendotti and Carri, 2004; Bruijn et al., 2004; Xu et al., 2004). In animal models, mitochondrial abnormalities were seen in motor neurons of mice or rats expressing the SOD1 mutations $SOD1^{G93A}$ (Dal Canto and Gurney, 1994; Jaarsma et al., 2001; Howland et al., 2002) and $SOD1^{G37R}$ (Wong et al., 1995), but similar pathology was not detected in motor neurons expressing other types of mutant SOD1 (Bruijn et al., 1997; Nagai et al., 2001). Furthermore, Andreassen et al. (2000) reported that heterozygous loss of SOD2 exacerbates disease in mutant SOD1 transgenic mice. Recent studies show that mutant SOD1, rather than abrogating function, acquires a toxic function and that mutant SOD1 expression is required in both neurons and glia cells to induce motor neuron degeneration (Gong et al., 2000; Pramatarova et al., 2001; Lino et al., 2002; Clement et al., 2003). The present study also is consistent with a possible importance of interplay between neurons and glia cells in motor neuron survival.

In an ALS mouse model, expression of the neuronal isoform of nitric oxide synthase (nNOS) is increased in astrocytes surrounding motor neurons in the spinal cord and brainstem (Cha et al., 1998). Also increased nitrotyrosine labeling in motor neurons and in the ventral horn has been reported in ALS and mutant SOD1-expressing mouse models (Abe et al., 1995; Beal et al., 1997; Ferrante et al., 1997; Cha et al., 2000). In the present study, we did not find any nitrotyrosine immuno-positive cells in the brain and spinal cord of 9-month-old $SOD2^{lox/lox}$;$Cre^{slow/-}$ mice. Furthermore, neither signs of reactive gliosis (GFAP-IR) nor peroxynitrite-mediated oxidative damage (nitrotyrosine-IR) in astrocytes surrounding SOD2-deficient motor neurons were evident. We speculate that elevated levels of $O_2^{\bullet-}$ in motor neurons is not by itself enough to trigger chronic cell injury, but NO produced from neighboring astrocytes resulting in peroxynitrite production may be a further requirement to trigger ROS-induced toxicity.

Axonal disorganization and reduced slow axonal transport are well-known hallmarks of ALS. Although our present results indicate that loss of SOD2 function is not by itself sufficient to kill motor neurons in vivo, it does modify axonal susceptibility to nerve injury. Recently Vande Velde et al. (2004) reported that Wld^S protein, the dominant neuroprotective factor that markedly delays Wallerian axonal degeneration after nerve injury, does not prevent SOD1-mediated motor neuron loss when introduced the Wld^S mutation into the $SOD1^{G37R}$ or $SOD1^{G85R}$ ALS mouse models. These results show that inhibiting axonal degeneration is not